

ARTICLE

The architecture of invaginating rod synapses slows glutamate diffusion and shapes synaptic responses

Wallace B. Thoreson^{1,2}, Thomas M. Bartol³, Nicholas H. Conoan⁴, and Jeffrey S. Diamond⁵

Synapses of retinal rod photoreceptors involve deep invaginations occupied by second-order rod bipolar cell (RBP) and horizontal cell (HC) dendrites. Synaptic vesicles are released into this invagination at multiple sites beneath an elongated presynaptic ribbon. To study the impact of this architecture on glutamate diffusion and receptor activity, we reconstructed four rod terminals and their postsynaptic dendrites from serial electron micrographs of the mouse retina. We incorporated these structures into anatomically realistic Monte Carlo simulations of neurotransmitter diffusion and receptor activation. By comparing passive diffusion of glutamate in realistic structures with geometrically simplified models, we found that glutamate exits anatomically realistic synapses 10-fold more slowly than previously predicted. Constraining simulations with physiological data, we modeled activity of EAAT5 glutamate transporters in rods, AMPA receptors on HC dendrites, and metabotropic glutamate receptors (mGluR6) on RBP dendrites. Simulations suggested that ~3,000 EAAT5 populate rod membranes. While uptake by surrounding glial Müller cells retrieves most glutamate released by rods, binding and uptake by EAAT5 influence RBP kinetics. Glutamate persistence allows mGluR6 on RBP dendrites to integrate the stream of vesicles released by rods in darkness. Glutamate's tortuous diffusional path confers quantal variability, as release from nearby ribbon sites exerts larger effects on RBP and HC receptors than release from more distant sites. Temporal integration supports slower sustained release rates, but additional quantal variability can impede postsynaptic detection of changes in release produced by rod light responses. These results show an example of the profound impact that synaptic architecture can have on postsynaptic responses.

Introduction

Rod photoreceptor synaptic terminals, termed spherules due to their bulbous shape, are structurally distinct from most other central synapses. The presynaptic active zone, which contains a platelike ribbon structure tethering dozens of synaptic vesicles, apposes postsynaptic dendrites of multiple second-order neurons that terminate deep within an invagination into the rod spherule (Fig. 1 A). Each synapse is typically occupied by two rod bipolar cell (RBP) dendrites and two horizontal cell (HC) dendrites that extend further into the invagination to flank the synaptic ridge. Absorption of even just a single photon by rhodopsin causes rods to hyperpolarize, temporarily decreasing the rate at which glutamate-filled vesicles are released at sites along the base of the ribbon (Moser et al., 2020; Thoreson, 2021). The resulting decrease in glutamate levels in the synaptic cleft alters the activity of glutamate receptors on RBP and HC dendrites. Here, we investigated how the complex architecture of this invaginating synapse influences the dynamics of glutamate diffusion following its release and, consequently, the synaptic responses of postsynaptic neurons.

Our understanding of glutamate dynamics at rod spherules has been shaped by work in which the dimensions of the rod synapse were measured and incorporated into geometrically simplified analytical diffusion models (Rao-Mirotznik et al., 1995, 1998). The resulting analysis argued that glutamate is cleared from the synaptic cleft in only a few milliseconds, suggesting that vesicles act independently on postsynaptic dendrites as discrete quanta rather than being integrated over time in the cleft. It also suggested that postsynaptic RBP and HC dendrites all experience a similar rapid change in glutamate concentration following the release of a synaptic vesicle by the rod. Here, we have tested whether these results hold in a diffusion model incorporating realistic synaptic architecture. We obtained serial block-face scanning electron micrographs (SBFSEM) of mouse retina and reconstructed four rod spherules along with their postsynaptic contacts. We imported these realistic structures into MCell4, a Monte Carlo simulation program that represents neurotransmitter diffusion and receptor/transporter kinetics as stochastic processes (Stiles et al., 1996; Franks

¹Truhlsen Eye Institute and Department of Ophthalmology and Visual Sciences, University of Nebraska Medical Center, Omaha, NE, USA; ²Department of Pharmacology and Experimental Neuroscience, University of Nebraska Medical Center, Omaha, NE, USA; ³Computational Neurobiology Laboratory, The Salk Institute, La Jolla, CA, USA; ⁴Electron Microscopy Core, University of Nebraska Medical Center, Omaha, NE, USA; ⁵Synaptic Physiology Section, Division of Intramural Research, National Institute of Neurological Diseases and Strokes, Bethesda, MD, USA.

Correspondence to Wallace B. Thoreson: wbthores@unmc.edu; Thomas M. Bartol: bartol@salk.edu; Jeffrey S. Diamond: diamondj@nih.gov.

© 2025 Thoreson et al. This article is distributed under the terms as described at https://rupress.org/pages/terms102024/.





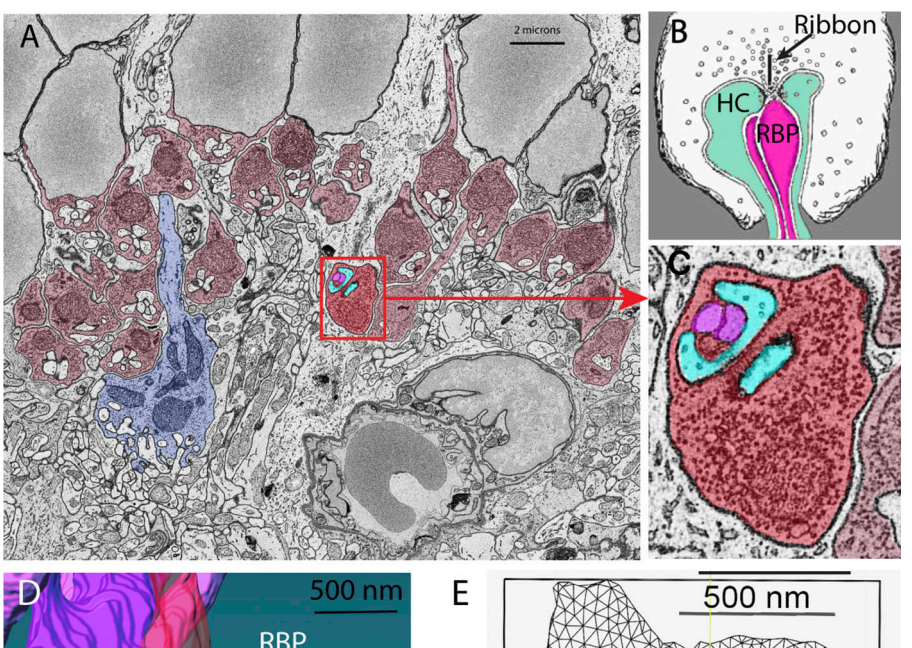
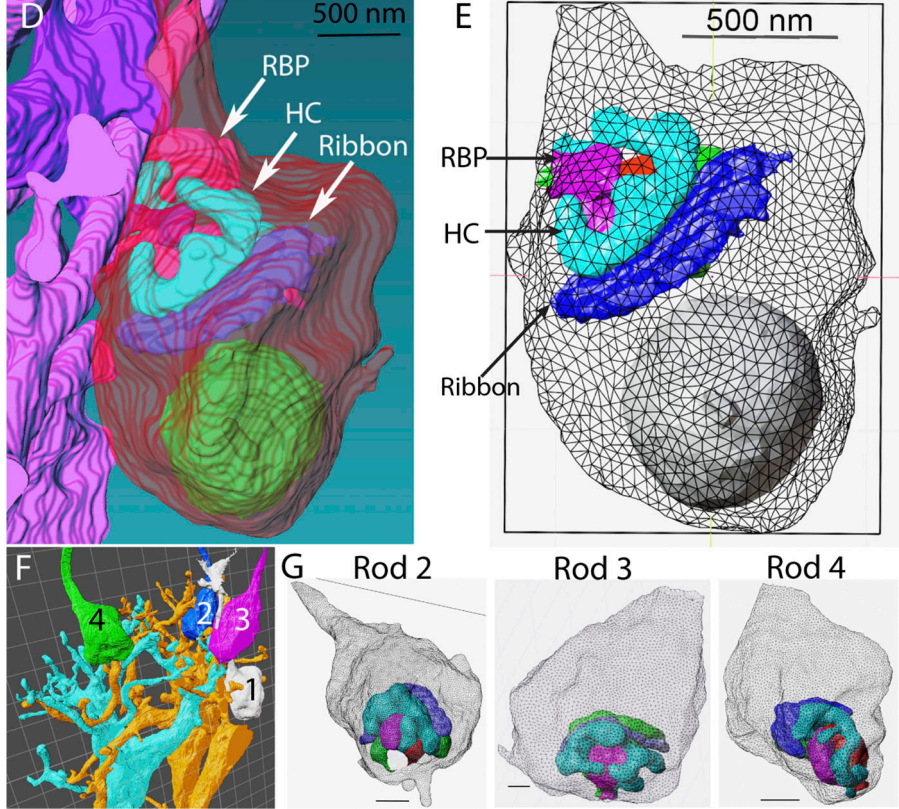


Figure 1. Model construction. (A) Example of an SBFSEM. Rod terminals are colored in red; cone terminal is colored in blue. Rod 1 used for reconstruction is shown in brighter red. (B) Diagram of an invaginating rod synapse. Vesicles surround the synaptic ribbon. RBP dendrites are in magenta, and HC dendrites are in turquoise. Modified under a Creative Commons License from Webvision (http://webvision.med.utah. edu/). (C) Magnified image of rod 1. Postsynaptic HC dendrites are in turquoise, and RBP dendrites are in magenta. (D) Reconstructed rod 1 terminal along with HC and RBP dendrites. The synaptic ribbon (dark blue) and mitochondrion (green) are also shown. (E) Mesh structures of the same cells. (F) Illustration of four reconstructed rod spherules (rods 1-4) with two RBPs (blue and yellow). (G) Mesh structures of rods 2-4 along with the postsynaptic HC and RBP dendrites. Scale bars = 500 nm. Details of these mesh structures are provided in Table 1.



et al., 2002; Garcia et al., 2022; Kerr et al., 2008; Husar et al., 2022, *Preprint*). We used MCell4 to evaluate the effects of synaptic geometry on passive glutamate diffusion, glutamate uptake by transporters, and the activation of postsynaptic glutamate receptors.

Simulated rod membranes were populated with type 5 excitatory amino acid transporters (EAAT5) (Arriza et al., 1997; Eliasof et al., 1998; Gehlen et al., 2021; Pow and Barnett, 2000). EAAT5 retrieves a fraction of synaptically released glutamate (Hasegawa et al., 2006), although most uptake appears to be accomplished by EAAT1 in Müller glial membranes (Eliasof et al., 1998; Rauen et al., 1996, 1998; Barnett and Pow, 2000;

Pow et al., 2000; Harada et al., 1998; Sarthy et al., 2005; Fyk-Kolodziej et al., 2004; Derouiche, 1996). The EAAT5 transport cycle activates a large anion current ($I_{A(glu)}$) (Arriza et al., 1997; Grant and Werblin, 1996; Schneider et al., 2014) that can be used as a reporter for presynaptic glutamate release (Szmajda and Devries, 2011; Hays et al., 2020). An existing kinetic model of EAAT2 (Kolen et al., 2020) was modified to represent EAAT5 and reproduce $I_{A(glu)}$ recorded from rods in response to singlevesicle release events (Kolen et al., 2020). Simulated HC membranes were populated with AMPA receptors (AMPARs) (Bartol et al., 2015; Jonas et al., 1993; Lu et al., 2009), modified to reproduce miniature excitatory postsynaptic currents (mEPSCs)



recorded in HCs. RBP membranes were populated with mGluR6, which closes TRPM1 cation channels via a G_o -type G protein-mediated intracellular signaling pathway (Schneider et al., 2015; Koike et al., 2010a) so that a reduction in glutamate release depolarizes RBPs.

Our simulations revealed that glutamate takes 10 times longer to exit an anatomically realistic synaptic cleft than suggested previously by a geometrically simplified model (Rao-Mirotznik et al., 1998). This longer lifetime at postsynaptic receptors enhances temporal integration in the RBP and suggests that slower rod release rates than previously predicted can maintain the RBP membrane potential in darkness. Slower diffusion kinetics also leads to greater variability in glutamate concentration transients and receptor activation that depends strongly on the relative locations of the released vesicles along the ribbon and the postsynaptic dendrites in the cleft. These additional sources of variability complicate the challenging task facing RBPs of discriminating small rod light responses from synaptic noise, inviting a reconsideration of optimal strategies for detection at the scotopic threshold.

Materials and methods

Anatomical reconstructions and MCell simulations

Serial block-face images were obtained using an Apreo VS scanning electron microscope (SEM; Thermo Fisher Scientific). The tissue was fixed by immersion with standard EM fixative (2% glutaraldehyde, 2% paraformaldehyde, 0.1 M phosphate buffer). We sectioned a volume of 14.3 \times 20.6 \times 24 μm . Voxel dimensions are 6 \times 6 \times 40 nm, and each image consisted of 3,435 \times 4,000 pixels.

3D reconstructions were performed using Amira software (RRID:SCR_007353). Reconstructed cell membranes were converted to 3D triangular mesh structures using the CellBlender add-on to the 3D computer graphics program Blender (RRID: SCR_008606, Fig. 1). The volume, surface area, and faces of the mesh structures for each of the four rods and their postsynaptic partners are provided in Table 1. Simulations were performed with these reconstructions using the Monte Carlo simulation software MCell4 (RRID:SCR_007307) (Husar et al., 2024) that simulates molecular diffusion as a pseudorandom walk according to an assigned diffusion constant. Glutamate molecules diffuse in three dimensions in extracellular space and can interact stochastically with immobile receptors and transporters located on membrane surfaces. The behavior of each individual glutamate transporter and receptor was represented by stochastic transitions between states within an individual Monte Carlo model.

To simulate EAAT5 glutamate transporters, we adjusted the kinetics, density, and location of simulated transporters to reproduce the amplitude and time course of $I_{A(glu)}$ recorded in rods in response to single-vesicle release events. Simulated rod membranes were densely populated with EAAT5 ($10,000/\mu m^2$) (Hasegawa et al., 2006) and represented by a simplified model for EAAT2 (Kolen et al., 2020). Glutamate-binding and -unbinding rates were adjusted to match the rising phase of averaged single-vesicle $I_{A(glu)}$ events (Fig. S1 A) and maintain the

10 μ M EC₅₀ measured for EAAT5 in mouse rods (Thoreson and Chhunchha, 2023). We tested ON rates from 1 × 10⁶ M/s to 1 × 10⁹ M/s. ON rates of 1 × 10⁸ M/s and 1 × 10⁹ M/s produced reasonable fits to the initial inward deflection in $I_{A(glu)}$ (Fig. S1 A). However, simulations with an ON rate of 1 × 10⁹ M/s were more sensitive to EAAT5 placement than fits with 1 × 10⁸ M/s (compare panels D and E in Fig. S2) and yielded fewer channel openings than predicted from single-vesicle currents. To match the single-vesicle $I_{A(glu)}$ decay when using an ON rate of 1 × 10⁸, we increased by threefold the transition rate constant of $T_{out}^*Glu \rightarrow T_{int}^*Glu$.

We examined the effects of EAAT5 location on $I_{A(glu)}$ kinetics by placing EAAT5 in four different regions: rod membrane deep within the invagination adjacent to RBP tips, the neck of invagination (Neck), surrounding the exit of the invagination (Exit), and distributed throughout the entire cleft (Cleft) (Fig. S1 C). With an ON rate of 1×10^8 M/s, placing EAAT5 adjacent to RBP dendritic tips (turquoise) or distributing transporters throughout the cleft (purple) both produced similar responses that provided a reasonable match to actual $I_{A(glu)}$ events. Placing EAAT5 only in the neck of the invagination (green trace) or outside the cleft (deep blue) yielded decay kinetics that was faster than actual $I_{A(glu)}$ events, as well as yielded fewer channel openings. Since distributing receptors throughout the cleft yielded comparable results to placing them deep within the invagination, we chose the former for subsequent simulations.

To estimate the number of EAAT5 in rods, we began with evidence that single-vesicle I_{A(glu)} events average 4.5 pA (Thoreson and Chhunchha, 2023). We calculated the anion driving force by plotting voltage-dependent changes in the average amplitude of single-vesicle $I_{A(glu)}$ events, fitting these data with a straight line. The reversal potential predicted from these measurements averaged -8.2 ± 0.62 mV (n = 6 rods). The holding potential of -70 mV therefore generates a driving force of 62 mV. The single-channel conductance of EAAT5 measured with nitrate as a charge carrier was found to be 0.6 pS (Schneider et al., 2014), and glutamate transporters in salamander rods show a single-channel conductance with chloride as the charge carrier of 0.7 pS (Larsson et al., 1996). SCN⁻ is more permeable than chloride or nitrate, so we assumed a larger single-channel conductance of \sim 1 pS. These values suggest that \sim 72 anion channels are open at the peak of a single-vesicle release event.

The maximum open probability of EAAT2 anion channels has been estimated at ~0.06 (Kolen et al., 2020). To calculate the open probability for anion channels achieved in our simulations, we divided the number of open anion channels by the total number of glutamate-bound states. We used the same rate for entry into the open state from $T_{\rm int}^*$ Glu as in the earlier model for EAAT2 (9,566/s) (Kolen et al., 2020). Assuming that channels are equally likely to exit the open state (i.e., open state \rightarrow $T_{\rm int}^*$ Glu = 9,566/s), we obtain an open probability of 0.077. This seems reasonable given that EAAT5 $I_{\rm A(glu)}$ are thought to have a larger open probability than EAAT2.

Like other metabotropic glutamate receptors, mGluR6 forms a homodimer and both members need to bind glutamate for G protein activation (Pin and Acher, 2002; Levitz et al., 2016). We therefore modeled mGluR6 activation as two sequential



Table 1. Details of mesh structures of rods, HC dendrites, and RBP dendrites used for simulations

	Rod 1	Rod 2	Rod 3	Rod 4
Surface area (μm²)	29.15	27.67	32.29	26.13
Volume (μm³)	5.94	5.024	6.576	4.771
Faces	6,580	14,498	57,802	30,384
Cleft volume (µm³)	0.564	0.572	0.6056	0.448
Extracellular cleft volume (μm³)	0.1125	0.06	0.074	0.057
ECV	0.2	0.11	0.12	0.13
HC dendrite 1				
Surface area (μm²)	2.758	3.272	2.726	2.382
Volume (μm³)	0.1674	0.1945	0.1763	0.114
Faces	2040	4754	2388	1914
HC dendrite 2				
Surface area (μm²)	2.827	3.123	3.213	2.272
Volume (μm³)	0.1894	0.1758	0.2228	0.1337
Faces	1088	7020	5530	2418
BP dendrite 1				
Surface area (μm²)	0.7964	1.2167	1.0288	1.1962
Volume (μm³)	0.03475	0.07234	0.06593	0.07867
Faces	662	3084	5038	602
BP dendrite 2				
Surface area (μm²)	0.6539	1.041	1.0622	1.17
Volume (μm³)	0.03208	0.069	0.06686	0.06456
Faces	1422	714	4832	568
BP dendrite 2b				
Surface area (μm²)	0.6792			
Volume (μm³)	0.0276			
Faces	1732			

glutamate-binding steps, considering the doubly bound mGluR6 dimer to be the activated receptor (Fig. S2). We assumed that the decay in the number of active mGluR6 receptors (i.e., decay of the doubly bound state) following the release of a single vesicle should be at least as fast as the inward current evoked in RBPs by a saturating light flash (20–80% increase: 25.4 ± 1.9 ms; SEM, n =19; J. Pahlberg, unpublished data). As illustrated in Fig. S2, we tested different rate constants and achieved a similar rate of decay in the doubly bound state using an OFF rate for glutamate unbinding of 500/s (20-80%: rod 1, 27 ms; rod 2, 50 ms; rod 3, 36 ms; rod 4, 28 ms). Combining this OFF rate with an ON rate for the initial glutamate-binding step of 1e8 M/s yielded a steadystate EC_{50} of 14 μ M (Fig. S2), matching that measured by the displacement of glutamate from mGluR6 (12.3 µM [Pin and Acher, 2002]). These parameters also yielded a slope factor of 1.4, similar to changes in mGluR6-mediated responses as a function of light intensity in dark-adapted RBPs (Sampath and Rieke, 2004; Berntson et al., 2004).

To simulate HC AMPARs, we used a kinetic model of AMPARs empirically derived from hippocampal neurons (Jonas et al., 1993). The original parameters were developed to fit data

obtained at room temperature and later modified for a temperature of 34°C (Bartol et al., 2015).

Release from photoreceptors varies linearly with I_{Ca} (Thoreson et al., 2004), and so we estimated voltage dependence of release rates in rods from changes in I_{Ca} . For the voltage dependence of I_{Ca} , we used a Boltzmann function modified for driving force with an activation midpoint (V_{50}) obtained from a sample of mouse rods (–31.5 mV; n=8) along with a reversal potential of +41 mV (Grassmeyer and Thoreson, 2017) and a slope factor of 9 (Haeseleer et al., 2016).

Other analysis and data visualization procedures were performed using Clampfit 10, GraphPad Prism 9, Adobe Illustrator, and Adobe Photoshop software.

Mice

For electrophysiology studies, we used mice of both sexes aged between 4 and 8 wk. Euthanasia was performed by ${\rm CO_2}$ asphyxiation followed by cervical dislocation in accordance with AVMA Guidelines for the Euthanasia of Animals. Animal care and handling protocols were approved by the University of Nebraska Medical Center Institutional Animal Care and Use



Committee. Experiments were conducted using C57BL/6] mice.

Whole-cell recordings

Whole-cell recordings of rods were obtained using flat-mount preparations of isolated retina. Eyes were enucleated after euthanizing the mouse and placed in Ames' medium (RRID: SCR_013653; US Biological) bubbled with 95% O₂/5% CO₂. The cornea was punctured with a scalpel and the anterior segment removed. The retina was isolated after cutting optic nerve attachments. We then made three or four fine cuts at opposite poles and flattened the retina onto a glass slide in the perfusion chamber with photoreceptors facing up. The retina was anchored in place with a brain slice harp (cat. no. 64-0250; Warner Instruments). To expose rod inner segments in the flat-mount retina, we gently touched the photoreceptors with a piece of nitrocellulose filter paper and then removed it to pull away adherent outer segments. The perfusion chamber was placed on an upright fixed-stage microscope (E600FN; Nikon) equipped with a 60× water-immersion, long working distance objective (1.0 NA). The tissue was superfused with room temperature Ames' solution bubbled with 95% $O_2/5\%$ CO_2 at \sim 1 ml/min.

Whole-cell recordings were performed using either an Axopatch 200B amplifier (RRID:SCR_018866; Molecular Devices) with signals digitized by a DigiData 1550 interface (Molecular Devices) using pCLAMP 10 software or HEKA EPC-10 amplifier (RRID:SCR_018399) and Patchmaster software (RRID:SCR_000034; Lambrecht). Currents were acquired with filtering at 3 kHz.

Patch recording electrodes were pulled on a Narishige PP-830 vertical puller using borosilicate glass pipettes (1.2 mm outer diameter, 0.9 mm inner diameter with internal filament; World Precision Instruments). Pipettes had tip diameters of 1–2 μ m and resistances of 10–15 $M\Omega$. Rod inner segments were targeted with positive pressure using recording electrodes mounted on Huxley–Wall or motorized micromanipulators (MP225; Sutter Instruments).

Rod ribbons are surrounded by the glutamate transporter EAAT5 (Arriza et al., 1997; Eliasof et al., 1998; Hasegawa et al., 2006), and glutamate reuptake into rods by these transporters activates a large $I_{A(glu)}$ (Arriza et al., 1997; Grant and Werblin, 1996; Schneider et al., 2014). $I_{A(glu)}$ is thermodynamically uncoupled from the transport process (Machtens et al., 2015). Glutamate transporter $I_{A(glu)}$ can be observed in rods using Cl^- as the principal anion (Hays et al., 2020), but are enhanced by replacing Cl^- with a more permeable anion such as thiocyanate (SCN $^-$) in the patch pipette (Eliasof and Jahr, 1996). The intracellular pipette solution for these experiments contained the following (in mM): 120 KSCN, 10 TEACl, 10 HEPES, 1 CaCl $_2$, 1 MgCl $_2$, 0.5 Na-GTP, 5 MgATP, 5 EGTA, 5 phosphocreatine, pH 7.3. Voltages were not corrected for a liquid junction potential of 3.9 mV.

To record mEPSCs from HCs, horizontal slices of retina were prepared as described elsewhere (Feigenspan and Babai, 2017). Briefly, retinas were isolated and then embedded in 1.8% low gelling agarose (Sigma-Aldrich). Horizontal slices (200 μm thick) were cut parallel to the plane of the retina using a vibratome (RRID:SCR_016495; VT1000S; Leica Microsystems) at room temperature.

For HC recordings, we used a pipette solution containing the following (in mM): 120 K-gluconate, 10 TEACl, 10 HEPES, 5 EGTA, 1 $CaCl_2$, 1 $CaCl_2$, 0.5 NaGTP, 5 MgATP, 5 phosphocreatine, pH 7.2–7.3. HCs were identified visually and confirmed physiologically by the characteristic voltage-dependent currents, particularly prominent A-type K $^+$ currents (Feigenspan and Babai, 2017). In our initial recordings, the HC identity was confirmed anatomically by loading the cell with the fluorescent dye Alexa 488 (Invitrogen) through the patch pipette. Other chemical reagents were obtained from Sigma-Aldrich unless otherwise indicated.

Online supplemental material

Fig. S1 shows EAAT5 parameters and placement. Fig. S2 shows the kinetics of glutamate binding to mGluR6.

Results

Model construction

To create an anatomically detailed diffusion model of rod photoreceptor synapses, we first obtained a series of SBFSEM images from the outer retina of a C57Bl6J mouse (Fig. 1, A and B). By viewing consecutive sections at high magnification, we reconstructed four rod spherules along with their postsynaptic HC and RBP dendrites (Fig. 1 C). We then rendered the reconstructed synapses as a collection of 3D surfaces (Fig. 1 D) and imported them into MCell. The four reconstructed terminals had the same general structure but exhibited significant variability in geometric dimensions (Fig. 1, E–G and Table 1).

Rao-Mirotznik et al. (1998) modeled the cat rod synapse as a sphere with a narrow neck for the exit. We created similar models in MCell, configuring spheres with volumes to match the clefts of mouse rods 1 and 2 (Fig. 2 A, sphere models shown at the same scale as reconstructed terminals). Like the earlier model, these spheres emptied through a narrow neck ($r = 0.12 \mu m$, length = $0.1 \mu m$).

Estimates of the number of glutamate molecules filling each synaptic vesicle vary widely (Wang et al., 2019; Orrego and Villanueva, 1993; Takamori et al., 2006), so we chose a moderate value of 2,000 glutamate molecules. As mouse rod synaptic vesicles have an inner diameter of about 30 nm (Fuchs et al., 2014), 2,000 glutamate molecules would constitute ~250 mM, close to biochemical measurements of purified synaptic vesicles from the cortex (210 mM; Riveros et al., 1986).

Effects of synaptic geometry on passive diffusion of glutamate

We first simulated the release of 2,000 glutamate molecules from points at the apexes of the two spheres containing the cleft volumes of rods 1 and 2. Using a diffusion coefficient (D) describing free diffusion of glutamate in saline (D = 8 × 10⁻⁶ cm²/s; Rao-Mirotznik et al., 1998), our Monte Carlo simulations predicted rapid clearance from the synaptic cleft (τ = 0.88 and 0.46 ms for spheres 1 and 2, respectively; Fig. 2, B and C). Using a larger sphere that matched the cleft volume of a cat rod spherule (0.21 μ m³; Rao-Mirotznik et al., 1995), Monte Carlo simulations yielded a 1.6-ms time constant for glutamate clearance, close to the value of 1.7 ms predicted analytically by Rao-Mirotznik et al. (1998).



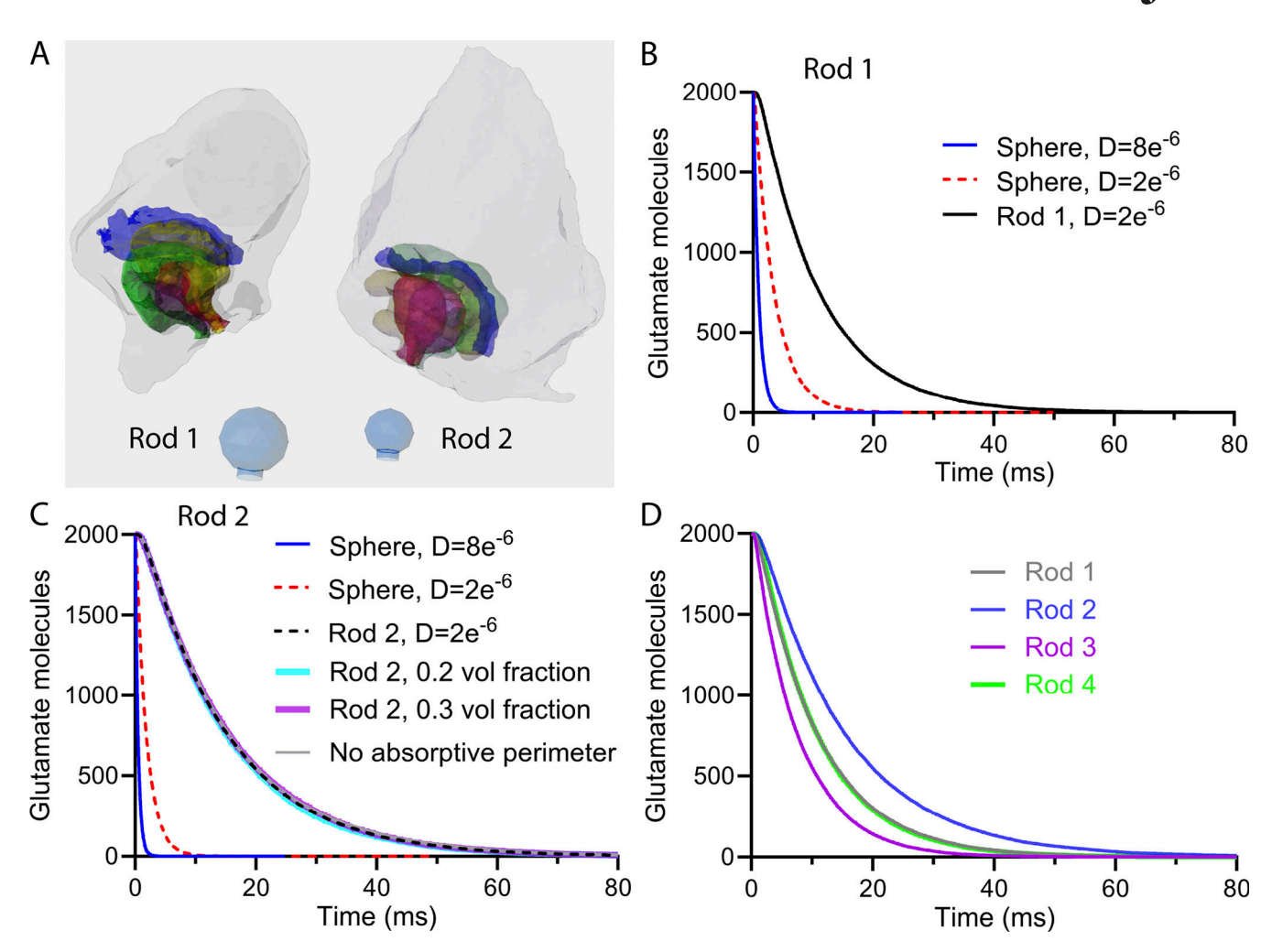


Figure 2. Simulations of passive glutamate diffusion comparing reconstructed rod spherules with simplified models that represented the extracellular synaptic volume as a sphere with a narrow neck for an exit. (A) Illustration of reconstructed rod spherules 1 and 2. HC dendrites are in yellow and green, BP dendrites are in red and magenta, and ribbons are in blue. Below each spherule is the corresponding sphere model containing the same extracellular volume shown at the same scale. (B) Plot of the number of glutamate molecules that remained after the release of a vesicle in the synaptic cleft of rod 1 (D = 2×10^{-6} cm²/s, black line) or a sphere with the same extracellular volume (D = 8×10^{-6} cm²/s, blue line; D = 2×10^{-6} cm²/s, dashed red line). We simulated release in rod 1 at a site just beneath the center of the ribbon. (C) Graph of the glutamate decline in a sphere with the same extracellular volume as the invaginating synapse of rod 2 (D = 8×10^{-6} cm²/s, blue line; D = 2×10^{-6} cm²/s, dashed red line). This graph also shows the decline in glutamate following the release of a vesicle beneath the center of the ribbon in rod 2 with volume fractions of 0.11 (D = 2×10^{-6} cm²/s, black line), 0.2 (turquoise line), and 0.3 (purple line). Eliminating an absorptive perimeter that simulates avid Müller cell uptake had no effect on the time course of decay (gray trace). (D) Comparison of passive glutamate decline in the four rod spherules. Fitting the decays with single exponentials yielded the following time constants: rod 1: 10.64 ms; rod 2: 14.10 ms; rod 3: 7.45 ms; and rod 4: 8.89 ms. Each trace is an average of 12 simulations run using different seed values.

Work at other central synapses indicates that glutamate diffusion in extracellular space at synapses is slower than in free solution (Nicholson et al., 1979; Nicholson and Hrabětová, 2017; Syková, 2004; Rusakov and Kullmann, 1998; Nielsen et al., 2004). Lowering D to account for the viscous tortuosity of extracellular space from 8 to 2×10^{-6} cm²/s (Franks et al., 2002) slowed diffusion and consequently glutamate clearance several-fold (Fig. 2, B and C).

We next analyzed the impact of realistic synaptic geometry by comparing results of the two-sphere models with simulations of single-vesicle release in the reconstructed rod synapses. Within the realistic geometry, we positioned the vesicle release site just beneath the ribbon at the center of the invagination. These simulations produced even slower glutamate clearance time constants (Fig. 2, B and C). Notably, the cross-sectional area of the extracellular space at the neck of the synaptic invaginations closely approximated that of the exit from the simplified spherical models, indicating that slower clearance from the reconstructed synapses was not due to greater constriction at the neck.

Given the larger extracellular volume fraction (ECV, α) of rod 1 compared with rod 2 (Table 1), we tested the effects of this parameter on our results. To do so, we shrank the postsynaptic dendrites in rod 2 to increase α from 0.11 to 0.2 and 0.3 and found that the time constant of glutamate decay remained the same (Fig. 2 C). Taken together, these results show that the geometric tortuosity introduced by the complicated anatomy of the invaginating rod synapse dictates the dynamics of



neurotransmitter diffusion (Rusakov and Kullmann, 1998; Nicholson and Hrabětová, 2017; Nielsen et al., 2004).

Müller glial cell processes envelope rod synapses and retrieve glutamate molecules that escape the cleft (Sarantis and Mobbs, 1992; Attwell et al., 1989; Rauen et al., 1998). To simulate avid Müller cell uptake, we wrapped the entire rod terminal with an absorptive mesh to remove any glutamate molecule that exited the synaptic cleft immediately. This absorptive perimeter had no effect on the time course of glutamate clearance compared with simulations in which escaping glutamate entered a large open volume (Fig. 2 C). This suggests that while Müller cell uptake is likely important for maintaining a steep glutamate diffusion gradient at the mouth of the synapse, it does not directly regulate the rate of glutamate clearance from the cleft.

We also examined passive glutamate diffusion at the other two reconstructed rod synapses. Rods 3 and 4 had similar cleft volumes and α compared with rod 2 (Table 1). As observed with rod 2, increasing α of rods 3 and 4 did not substantially affect the rate of glutamate clearance. Although rods 2, 3, and 4 all had similar cleft volumes, the rates of glutamate clearance ranged from 7.4 to 14 ms among them (Fig. 2 D). Interestingly, rods 1 and 4 exhibited similar simulated glutamate clearance rates, even though rod 1 has twice the extracellular volume (Fig. 2 D). These rod-to-rod differences further demonstrate the powerful influence of realistic geometric tortuosity on the kinetics of glutamate diffusion within invaginating rod synapses (Rusakov and Kullmann, 1998; Nicholson and Hrabětová, 2017). The combined effects of viscous and geometric tortuosity slow glutamate clearance from rod synapses 10-fold compared with the exit from a saline-filled sphere. The unexpectedly prolonged presence of glutamate in the cleft prompted us to simulate its interaction with synaptic glutamate transporters and receptors.

To predict glutamate concentrations achieved at RBP dendrites, Rao-Mirotznik et al. (1998) modeled the invaginating rod synapse as three slabs intersecting at 120°, with a vesicle release site positioned at the confluence of the slabs. Fig. 3 A shows a schematic of the invaginating synapse with a RBP dendrite terminating some distance below the ribbon release site, while the two HC dendrites flank the synaptic ridge. The model simulates this structure by using two slabs to represent the extracellular space between the rod and HC membranes, while the third slab represents the extracellular space above an RBP terminal (Fig. 3 A). We recreated this arrangement in MCell with each slab consisting of two planes separated by 16 nm, then simulated the release of 2,000 glutamate molecules at the vertex of this narrow cleft. We measured the number of glutamate molecules that entered a small measurement box (15 \times 100 \times 200 nm) placed 70 nm from the release site (Fig. 3 A). As predicted by Rao-Mirotznik et al., Monte Carlo simulations of the release of 2,000 molecules showed an abrupt rise and a rapid decline of glutamate within this region (Fig. 3 C). We compared this model with the four reconstructed synapses by placing a measurement box $(15 \times 100 \times 200 \text{ nm})$ just above RBP dendrites (e.g., Fig. 3 B). The proximity of the measurement box to the release site minimized the effects of tortuosity, and so we saw a similarly rapid rise and fast decay in the rod synapses (τ_{fast} = 0.114 ± 0.0217 ms; τ_{slow} = 0.589 ± 0.1394 ms; Fig. 4 C) and the planar

model (τ_{fast} = 0.081 ms; τ_{slow} = 0.558 ms). We converted the number of molecules in the measurement regions to concentration (Fig. 3 C). The peak concentration attained in the planar model was slightly lower than that attained in synapses (0.775 ± 0.3325 mM), but both are consistent with estimates of synaptic glutamate levels at rod synapses obtained by the use of lowaffinity antagonists (Kim and Miller, 1993; Cadetti et al., 2008).

Simulations of the glutamate transporter, EAAT5

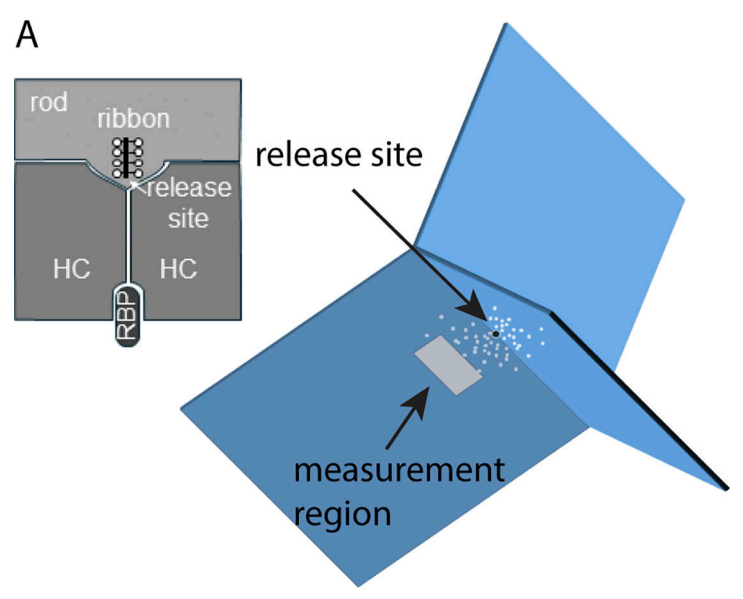
We next examined the influence of EAAT5 glutamate transporters, the principal glutamate transporters in rods (Eliasof et al., 1998; Arriza et al., 1997), on glutamate lifetime in the synaptic cleft (Fig. 4). Modifying a model for EAAT2 (Kolen et al., 2020), we adjusted the kinetics, density, and location of simulated transporters to reproduce the amplitude and time course of $I_{A(glu)}$ recorded in rods in response to single-vesicle release events (Fig. 4; see Materials and methods). The best fit to recorded EAAT5 currents was obtained by placing EAAT5 in the rod membrane within the synaptic cleft (see Materials and methods), consistent with immunohistochemical localization of this protein (Gehlen et al., 2021).

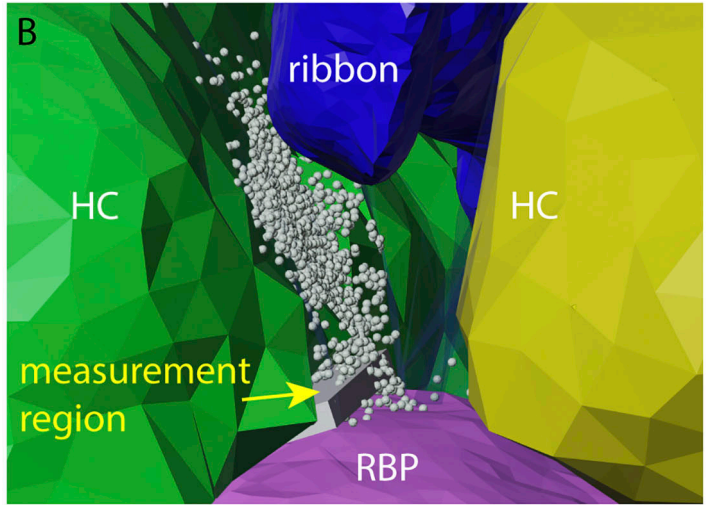
Rod $I_{A(glu)}$ responses evoked by photolytic uncaging of glutamate or strong depolarizing voltage steps reach a maximum of 12–13 pA (Mesnard et al., 2022b; Thoreson and Chhunchha, 2023), only three times larger than single-vesicle events, suggesting that EAAT5 can be saturated by the simultaneous release of as few as three vesicles. With this constraint in mind, we simulated the release of 10 vesicles and progressively reduced the number of EAAT5 until we achieved a state where responses showed saturating responses equivalent to 3–4 vesicles. With 3,000 EAAT5 distributed throughout the synaptic cleft, a single vesicle stimulated \sim 60 open anion channel openings, while the simultaneous release of 10 vesicles opened \sim 190 channels, showing saturation after the release of slightly >3 vesicles (Fig. 4 D). We therefore proceeded with simulations containing 3,000 EAAT5 in the rod membrane.

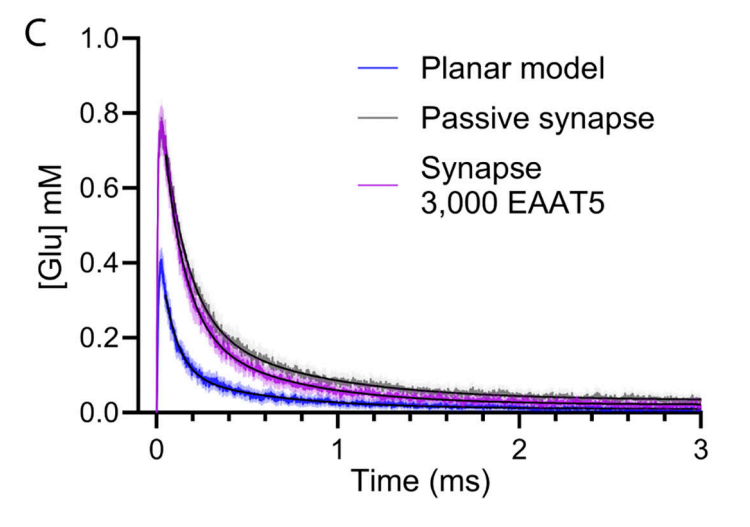
Fig. 4 E shows the impact on synaptic glutamate levels of uptake by 3,000 EAAT5 in rod 2. Following the release of a single vesicle, the simulations show that rapid binding of glutamate to EAAT5 speeds the initial decline in free glutamate. This is followed by a slower decline dictated by the rate of diffusion out of the synaptic cleft ($\tau_{\text{fast}} = 1.8 \text{ ms}$; $\tau_{\text{slow}} = 15 \text{ ms}$; n = 12trials). For a single-vesicle release event, the fast component accounted for 73% of the total decline in glutamate, consistent with binding of 1,460 glutamate molecules by 3,000 transporters. Rods are capable of multivesicular release events consisting of 10 or more vesicles (Hays et al., 2021). The presence of glutamate uptake by EAAT5 had only small effects on the kinetics of glutamate reaching RBP dendrites. Including 3,000 EAAT5 slightly accelerated glutamate decay in the measurement region placed just above the RBP dendrite in the previous figure (Fig. 4 C; τ_{fast} = 0.12 ms; τ_{slow} = 0.56 ms). When we simulated the simultaneous release of 10 vesicles, the fast component corresponding to glutamate binding of EAAT5 constituted a much smaller proportion of the total decline since the number of glutamate molecules (20,000) was much greater than the number of transporters (Fig. 4 F).

Glutamate release at invaginating rod synapses









To measure the maximum rate of glutamate uptake by 3,000 EAAT5, we simulated the release of 10 vesicles inside a closed synaptic cleft (rod 2; Fig. 4 F). The only exit available to glutamate in this simulation was uptake by EAAT5. Uptake settled to a constant rate of 63,390 glutamate molecules/s or 32 vesicles/s.

synaptic ridge (upper left) and an RBP dendrite terminating beneath the ribbon release site. The image at the lower right shows a simplified planar model of this synaptic arrangement that consists of three slabs intersecting at an angle of 120°. Each slab involves two planes separated by 16 nm to simulate a synaptic cleft. We simulated the release of 2,000 glutamate molecules at the vertex of this narrow cleft. We measured the number of glutamate molecules that entered a small measurement region (gray box, 15 × 100 × 200 nm) with the leading edge 70 nm from the release site. (B) Illustration of a reconstructed synapse (rod 1) with a measurement region (gray box, $15 \times 100 \times 200$ nm) placed just above an RBP dendrite (purple). HC dendrites are shown in yellow and green. The ribbon is in dark blue, and glutamate molecules are in sky blue. (C) Monte Carlo simulations of single-vesicle release showed an abrupt rise and a rapid decline of glutamate in measurement regions in the planar model (blue trace; average of 12 seeds) and four reconstructed synapses (purple trace; average of four rods, 12 seeds apiece). The red trace shows the change in glutamate observed when the rod models included active uptake by 3,000 EAAT5 distributed throughout the synaptic cleft. The measurement regions attained a peak concentration of 0.4 mM in the planar model and an average of 0.775 \pm 0.3325 mM in the four rod synapses. Decay kinetics was fit with two exponentials. Planar model: τ_{fast} = 0.081 ms; τ_{slow} = 0.558 ms. Passive glutamate decay in the four rod synapses: τ_{fast} = 0.114 ± 0.0217 ms; $\tau_{slow} = 0.589 \pm 0.1394$ ms. Decay in the rod synapses with active uptake by 3,000 EAAT5: τ_{fast} = 0.116 \pm 0.0238 ms; $\tau_{slow} = 0.644 \pm 0.1943 \text{ ms.}$

Figure 3. Comparing glutamate kinetics between a planar model and reconstructed rod spherules. (A) Schematic representation of an invaginating rod synapse that shows two HC dendrites flanking the

Performing the same simulation in a closed sphere with the volume of rod 2 yielded the same uptake rate. While EAAT5 can retrieve glutamate at rates up to 32 vesicles/s, glutamate declines much more rapidly when the synapse remains open, indicating that most of the glutamate diffuses out of the synaptic

9 of 20



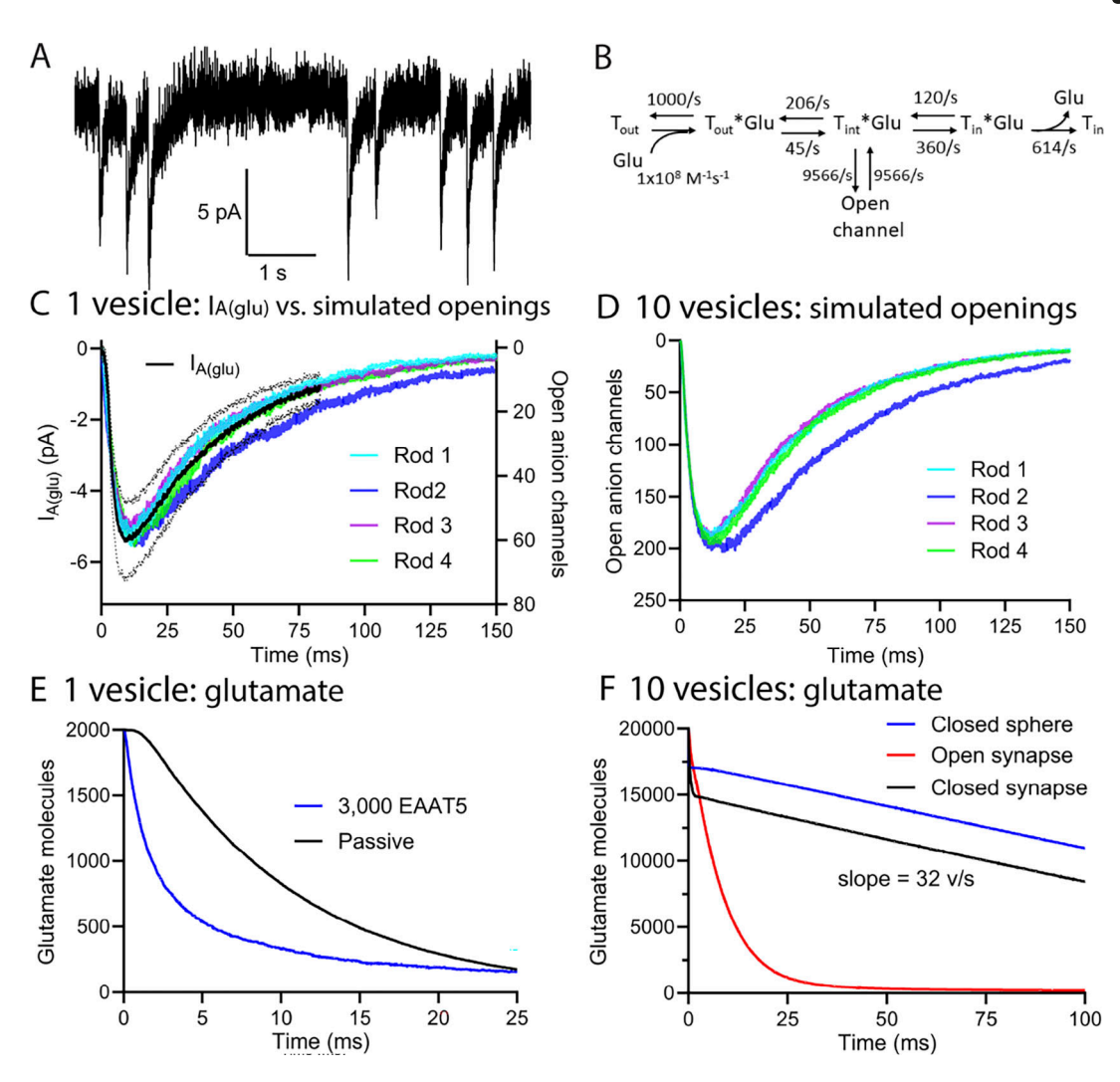


Figure 4. **Simulations of EAAT5 anion channel activity. (A)** Example of EAAT5 $I_{A(glu)}$ evoked by single-vesicle release events in a rod. **(B)** Reaction scheme for EAAT5 (modified from a model for EAAT2) (Kolen et al., 2020). **(C)** Colored traces show the average simulated EAAT5 anion channel activity in four rods following the release of a single vesicle. The black trace shows the average change in $I_{A(glu)}$ (\pm SD) evoked by single-vesicle release events in 15 rods (7–72 events/rod). **(D)** EAAT5 anion channel activity evoked in four rods by simulating the simultaneous release of 10 vesicles. **(E)** Comparison of the decline in glutamate molecules following the simulated release of a single vesicle with (blue trace) and without (black trace) 3,000 EAAT5 in rod 2. **(F)** Graph of the decline in glutamate following the simultaneous release of 10 vesicles in rod 2 with open (red trace) or closed (black trace) exits at the mouth of the synapse. The decline in a closed sphere with the same volume as rod 2 is plotted for comparison (blue trace). All simulations are the average of 12 runs with different seed values.

cleft, to be retrieved by Müller glia. Thus, our evidence suggests that EAAT5 in rods can take up functionally significant amounts of glutamate, as proposed by Hasegawa et al. (2006), but most of it is likely to be retrieved by extrasynaptic Müller cells, as suggested by others (Niklaus et al., 2017; Harada et al., 1998; Sarthy et al., 2005; Pow et al., 2000; Rauen et al., 1998).

Simulations of mGluR6 receptors on RBPs

Glutamate release at invaginating rod synapses

Glutamate released from rods acts at mGluR6 receptors on RBP dendrites (Nomura et al., 1994). Activating these receptors triggers a signaling cascade that leads to closing of TRPM1 cation channels (Morgans et al., 2010; Koike et al., 2010b). The signaling cascade is not understood in sufficient detail for a complete model, so we limited our model to the binding of glutamate to mGluR6. Class 3 metabotropic glutamate receptors—

including mGluR6—form obligate homodimers in which ligand binding to both members is needed to activate the G protein cascade (Levitz et al., 2016; Pin and Bettler, 2016). We placed 200 receptors at the tips of each of the two bipolar cell (BP) dendrites and modeled receptor activation as two sequential glutamate-binding steps, considering the doubly bound mGluR6 dimer to be the activated receptor (Fig. S2).

We compared simulations of mGluR6 activity in reconstructed rods with mGluR6 activity in the corresponding sphere model (Fig. 5). We placed 400 receptors in a transparent plane adjacent to a release site at the apex of the sphere matching the cleft volume of rod 2 (Fig. 5 A). This sphere is also close to cleft volumes of rods 3 and 4 (Table 1). We tested mGluR6 binding with and without 3,000 EAAT5 placed on the inner surface of the sphere. Nearly all of the mGluR6 receptors



in the sphere were rapidly bound following the release of a single glutamate-filled vesicle, and mGluR6 activation then decayed with a single time constant (10.1 ms; Fig. 5 C and Table 2) that actually became faster when EAAT5 was removed (6.6 ms; Fig. 5 D and Table 2). The slower decay in the presence of EAAT5 suggests that the transporters buffer glutamate, delaying its escape from the cleft and prolonging its interaction with mGluR6.

We compared these results with the kinetics and peak percentage of mGluR6 activated by a single vesicle in the four reconstructed rod spherules (Fig. 5 C). The peak percentage of receptors activated in the two postsynaptic BPs by a single vesicle ranged from 39% to 54%. For these simulations, we averaged the responses of both RBPs together. When we examined each of the two BPs individually, we saw a greater range in the peak level of mGluR6 activation that spanned 19-56%, with an average of 47%. In the presence of EAAT5, fitting the decay in mGluR6 activation in rods required two exponentials, with slow time constants ranging from 24 to 40 ms (Fig. 5 C and Table 2). In the absence of EAAT5, the decay in mGluR6 activity was well fit with a single exponential. Without EAAT5, mGluR6 activity following the release of a single vesicle attained a higher peak value and the response decayed with time constants ranging from 20 to 43 ms (Fig. 5 D and Table 2). Rod-to-rod differences and the slower decay of mGluR6 activation in reconstructed spherules compared with a simple sphere illustrate further the influence of synaptic geometry on response amplitude and kinetics.

Simulations of HC AMPARs

HC dendrites express AMPARs consisting of GluA2 and GluA4 subunits (Ströh et al., 2018; Hack et al., 2001). These two types show similar binding kinetics (Grosskreutz et al., 2003). We simulated HC AMPARs using an existing kinetic model for AMPARs that incorporates receptor binding, activation, and desensitization (Jonas et al., 1993; Bartol et al., 2015) (Fig. 6 A). To assess AMPAR kinetics in HCs, we averaged mEPSCs recorded from six mouse HCs (>50 events per cell). These mEPSCs exhibited rapid rise and decay phases (20-80% rise time = 0.6 ms, τ_{decay} = 0.81 ms; 95% confidence interval: 0.68–0.98 ms), as reported previously (Feigenspan and Babai, 2015). We placed 200 AMPARs on each of the dendritic tips of the two HCs and simulated the release of a single vesicle containing 2,000 glutamate molecules beneath the ribbon center (Fig. 6 B). Simulations in all four reconstructed synapses produced a good match to the actual decay of HC mEPSCs (Fig. 6 C). The rise times of simulated mEPSCs were faster than actual mEPSCs, possibly due to the imperfect voltage clamp of gap-junctionally coupled HCs $(R_s = 21.4 \pm 5.75 \text{ M}\Omega, R_m = 245 \pm 201 \text{ M}\Omega, C_m = 10.7 \pm 8.6 \text{ pF},$

As with mGluR6, we compared simulated AMPAR activation in the reconstructed rod synapses and in the sphere model (Fig. 6 D). Fig. 6 D illustrates four individual simulations of mGluR6 activity in rod 3 obtained using different seed values. Superimposed on these four-colored traces is the average AMPAR activity in the corresponding sphere model with 200 AMPARs placed in a transparent disk below the apical release site (n = 12 seeds; gray trace, Fig. 6 D). It is worth noting that

unlike mGluR6 where almost half of the receptors are activated by a single vesicle, a much smaller percentage of AMPARs are activated. Also, in contrast to mGluR6 activity that showed significantly different kinetics between the sphere and realistic synaptic models, AMPARs showed the same kinetics in the sphere and realistic synapse. Synaptic geometry thus has much less impact than intrinsic receptor kinetics on AMPAR activity.

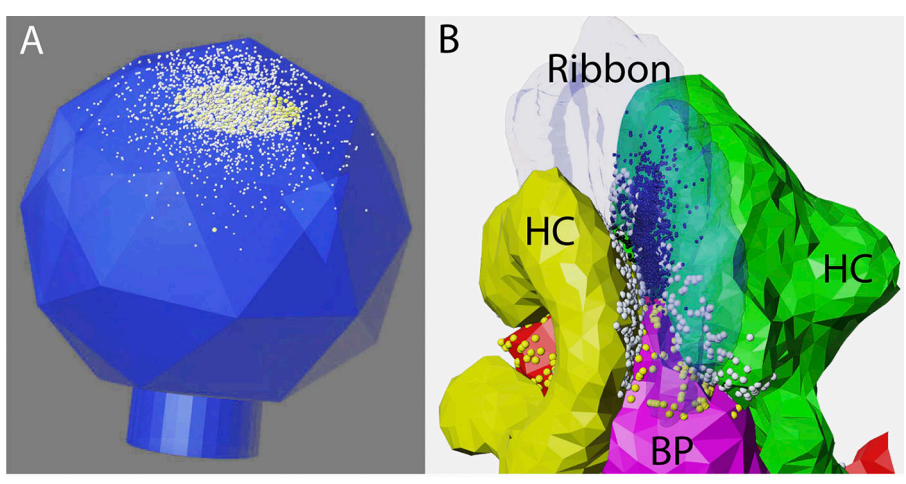
Release site location and dendritic anatomy

Synaptic vesicles can be released at many separate locations along the base of the presynaptic ribbon, suggesting that post-synaptic receptors may encounter widely varying glutamate concentration waveforms depending on their location relative to each released vesicle. We examined the effects of varying release site locations on EAAT5 anion channel activity by simulating release at three different sites along the ribbon: near the center and at both ends of the length of the ribbon. Within each rod, release at all three sites evoked similar changes in EAAT5 anion channel activity (Fig. 7), suggesting that the observed variability in single-vesicle $I_{A(glu)}$ events recorded in individual rods arises primarily from differences in the amount of glutamate released from each vesicle.

We next examined this issue from the standpoint of postsynaptic receptors in RBPs. We examined mGluR6 activity in both postsynaptic RBPs individually and compared six release sites with three sites on each face of the ribbon (arrows, Fig. 8). Activation of mGluR6 in the two rods varied with the release site location. For example, release indicated by the magenta arrow in rod 1 evoked a much smaller response (magenta traces) in BP1 than release at any other site. Large site-to-site differences remained evident even after we increased α of rod 2 from 0.11 to 0.3 (Fig. 8, insets beneath rod 2). These simulations show that differences in mGluR6 activation arise from geometric tortuosity and are not due to a more tightly confined extracellular space. Some synapses exhibited smaller differences between release sites. For both RBPs contacting rod 4 and BP2 beneath rod 2, mGluR6 activity was similar regardless of the release site location. Overall, simulations of single-vesicle release events activated 87.4 ± 37.1 mGluR6 receptors on each BP or 43.7 ± 18.5% (median: 46.1%) of the 500 receptors placed on each cell (n = 48 sites, responses at each site averaged from 25 seeds).

AMPAR activity in HC dendrites was even more sensitive to the release site location (Fig. 9). HCs typically showed stronger responses to release sites placed on the ribbon face nearest to their dendrites. Like BPs, similar site-to-site differences in AMPAR activation remained after we increased the volume fraction of rod 2 from 0.11 to 0.3, although the number of active AMPARs diminished due to the greater glutamate dilution (Fig. 9 B). On average, a single vesicle activated $4.7 \pm 4.0\%$ of the receptors (median: 3.7%; n = 48 release sites), with a range from 0.14 to 16.5% (Fig. 9 F). Fig. 9 E shows a histogram of the peak percentage of HC AMPARs and RBP mGluR6 activated by the release of individual vesicles at different ribbon sites. While single-vesicle release events activated a smaller percentage of AMPARs than mGluR6, the coefficient of variation (c.v.) for





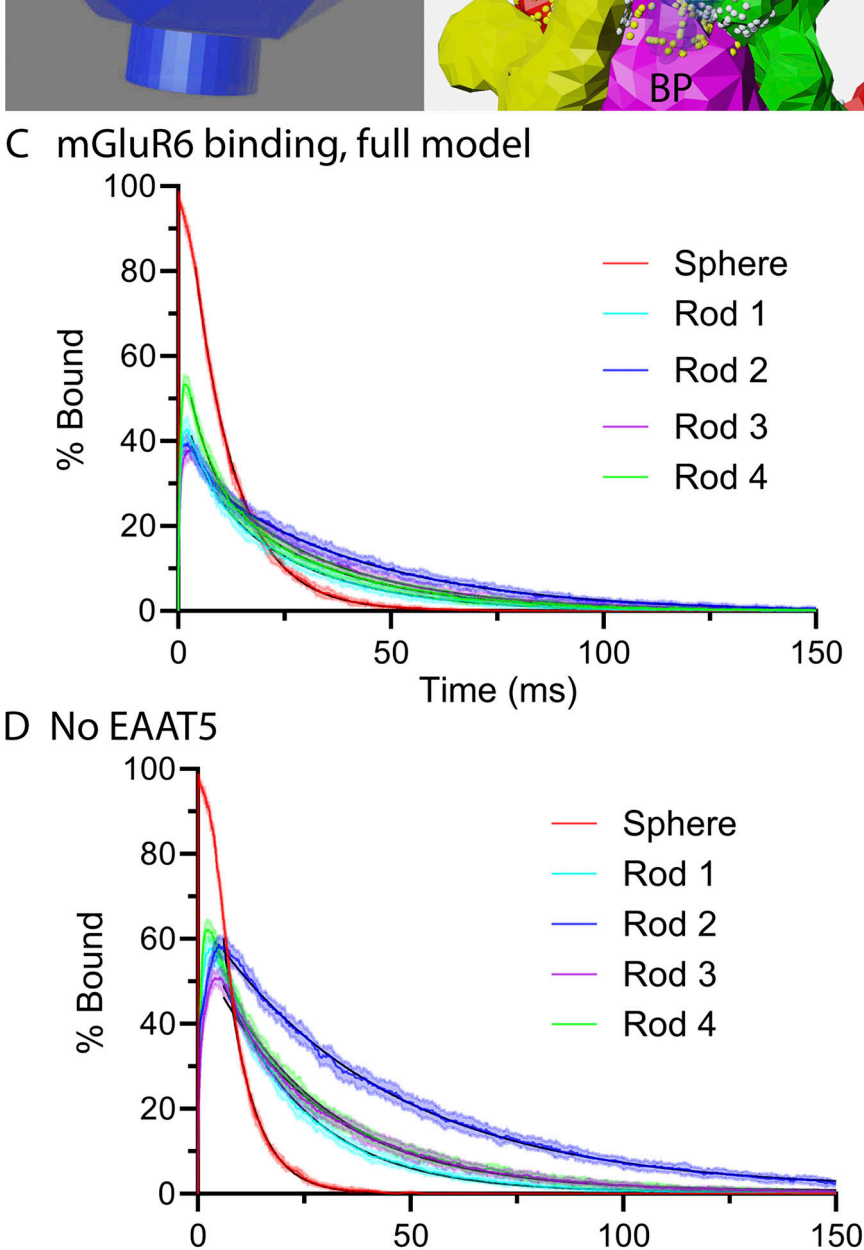


Figure 5. Activation of mGluR6 declines more slowly in rod spherules than in a similar-size sphere with a narrow neck. (A) Illustration of the sphere model for rod 2 showing 200 mGluR6 (yellow spheres) in a transparent plane just beneath a release site at the apex. Glutamate molecules following the release of a vesicle are shown in white. (B) Illustration of rod 1 with mGluR6 (yellow spheres) on BP dendrites (purple and red). Glutamate molecules are in white when in front of the semitransparent ribbon and shaded when behind the ribbon. (C) Activation of mGluR6 in the sphere and the four rod spherules in the presence of 3,000 EAAT5. The decay time courses in reconstructed rods were fit with two exponentials. The decay in the sphere was fit with a single exponential. Best-fit time constants are given in Table 2. (D) Activation of mGluR6 in the sphere and four rod spherules without EAAT5. All simulations in this figure are the average of 25 runs using different seed values

AMPARs as a function release site location was larger (0.85) than the c.v. for mGluR6 (0.42).

Time (ms)

Together, these results show that for glutamate receptors on both RBPs and HCs, release at one ribbon site may have a large effect on

one of the two postsynaptic cells and a small effect on the other, while release at a different site may have the opposite pattern. Thus, release site location and dendritic anatomy both have the potential to introduce significant sources of quantal variability at rod synapses.



Table 2. Best-fit parameters from Fig. 6 plotting mGluR6 activity evoked by single-vesicle release events in rods 1-4, as well as a sphere model

Activated mGluR6						
	With 3,000 EAAT5				No EAAT5	
	Peak % bound	τ _{fast} (ms)	% fast	τ _{slow} (ms)	Peak % bound	τ (ms)
Rod 1	42.1	4.8	33	24	53.9	20.4
Rod 2	40.6	4	29	40.1	58.3	42.9
Rod 3	39.3	7.2	18	30	50.8	26.7
Rod 4	53.5	5.4	48	28.2	56.4	26.2
Sphere	98.6			10.1	99	6.6
(volume of rods 2–4)						

Discussion

In this study, we investigated various aspects of synaptic function at the first synapse in the visual pathway using

anatomically realistic Monte Carlo simulations of rod spherules. Our results show that the combination of viscous and geometric tortuosity substantially delays glutamate's escape from the

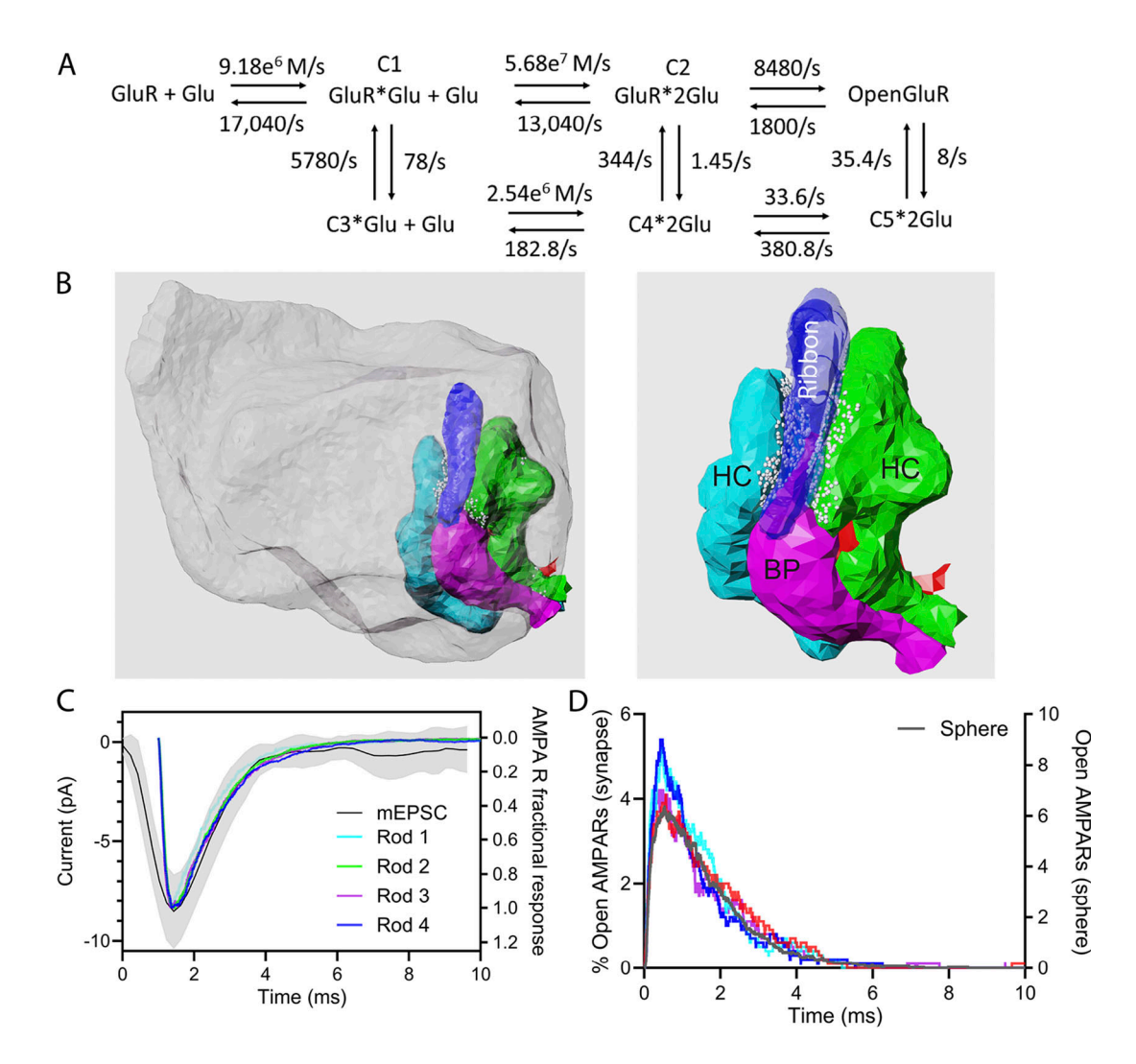


Figure 6. **Simulated AMPAR activity using a model for GluR2. (A)** Reaction scheme for AMPAR activation from Bartol et al. (2015). **(B)** Illustration of rod 1 spherule with BPs (purple and red), HCs (green and turquoise), and ribbon (semitransparent blue). AMPARs are shown as small white spheres. **(C)** Simulated single-vesicle AMPAR channel openings in four rod spherules compared with the average mEPSC recorded from mouse HCs (black trace ± SD). **(D)** Individual simulations run with four different seed values in rod 3 (colored traces). Superimposed on these traces is the average AMPAR activity observed with simulations in the corresponding sphere model (n = 25 seeds; black trace).

13 of 20



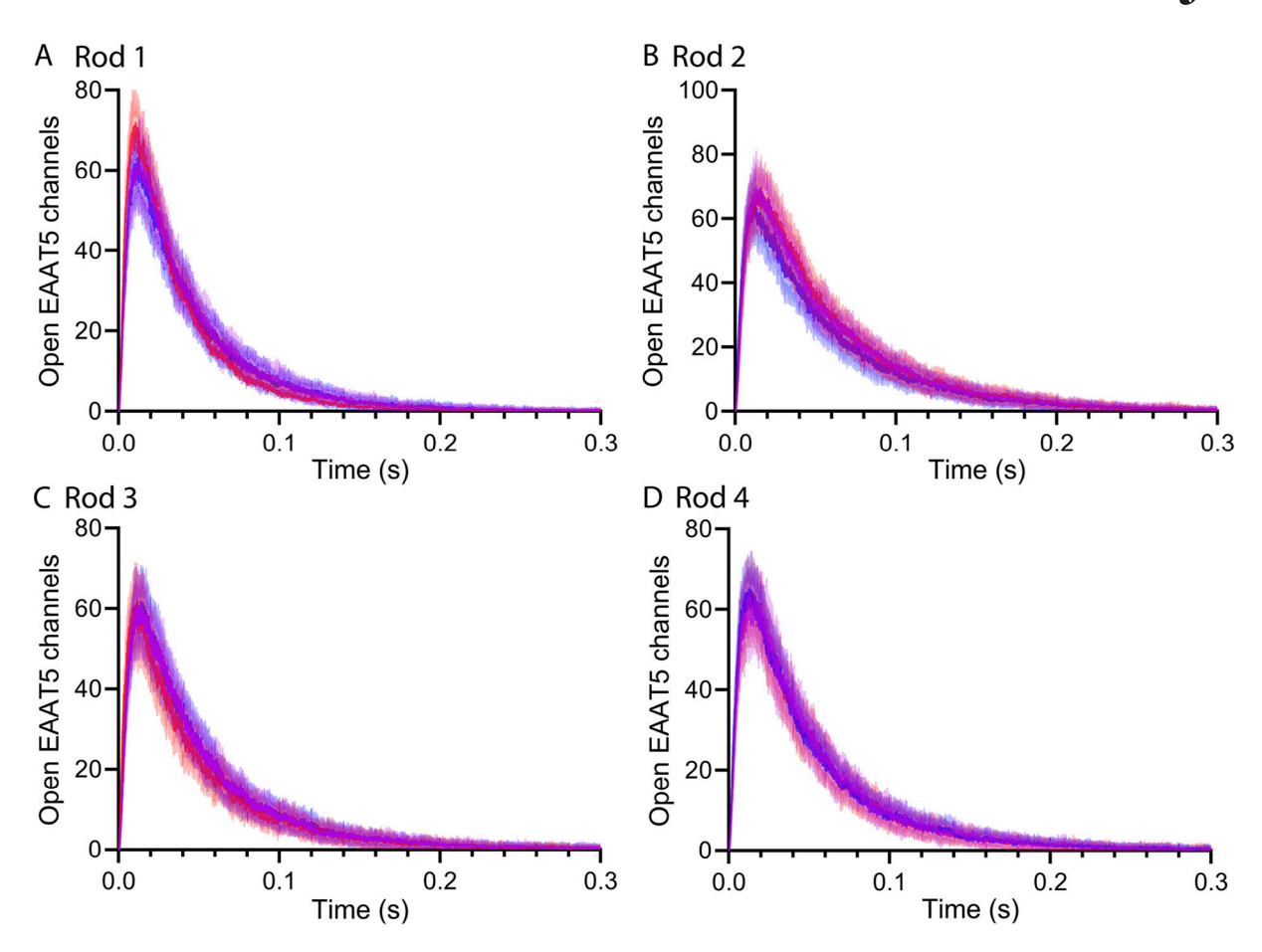


Figure 7. **Differences in release site location have an insignificant effect on EAAT5 anion channel activity. (A–D)** In all four rods, release was simulated at three different sites along each ribbon, one near the center (purple) and at two opposite edges (red and blue). Each trace shows the average ± SD of 25 simulations run with different seed values.

synaptic cleft of the invaginating rod synapse. While glutamate binding and uptake by EAAT5 help to lower glutamate levels, the persistence of glutamate in the invaginating synapse prolongs RBP mGluR6 receptor activity following vesicle release. The simulations also showed the significant impact of differences in cellular architecture and release site location on the amplitude and kinetics of synaptic responses at RBP and HC dendrites.

Effects of synaptic geometry

For simplicity, Rao-Mirotznik et al. represented the invaginating rod synapse as a sphere with a narrow cylindrical exit (Rao-Mirotznik et al., 1998). Our Monte Carlo simulations of diffusion within that simplified geometry replicated their analytical results showing that glutamate exits such a sphere very rapidly. With smaller mouse rods, glutamate departs a sphere even more quickly, with time constants of less than a millisecond. Replacing the diffusion coefficient for glutamate in saline with a diffusion coefficient that accounts for viscous tortuosity in the extracellular space (Nicholson et al., 1979; Nicholson and Hrabětová, 2017; Syková, 2004; Rusakov and Kullmann, 1998; Nielsen et al., 2004) slowed diffusion several-fold. Replacing the sphere with a realistic synapse incorporating the geometric tortuosity between cells slowed diffusion even further, yielding time constants for passive glutamate diffusion of ~10 ms. This slowing was not due to constriction at the

neck or an excessively small ECV in the reconstructed rod spherules. The impact of geometric tortuosity was evinced further by the twofold differences in the rate of glutamate exit among rods with similar cleft dimensions. While most rod spherules are outwardly similar to one another, they can differ significantly in the patterns of their dendritic invaginations (Tsukamoto and Omi, 2022). For example, rods in peripheral primate and cat retina often have two ribbons, rather than single ribbons as in the mouse retina (Migdale et al., 2003; Saha et al., 2023). These and other anatomic differences can have profound effects on glutamate diffusion kinetics.

mGluR6

To assess the effects of glutamate persistence on RBP responses, we modeled glutamate binding to mGluR6 receptors. Like other class C GPCRs, mGluR6 forms dimers in which agonists must bind both members for full G protein activation (Pin and Bettler, 2016; Levitz et al., 2016). We therefore considered mGluR6 active when bound to two glutamate molecules. Our simulations suggested that the release of glutamate from a single vesicle activates nearly half of the mGluR6 receptors on individual RBPs, i.e., at the steepest part of their concentration–response curve, thereby maximizing sensitivity to changes in glutamate release.

Our model did not incorporate downstream signaling pathways engaged by mGluR6 in which glutamate binding triggers



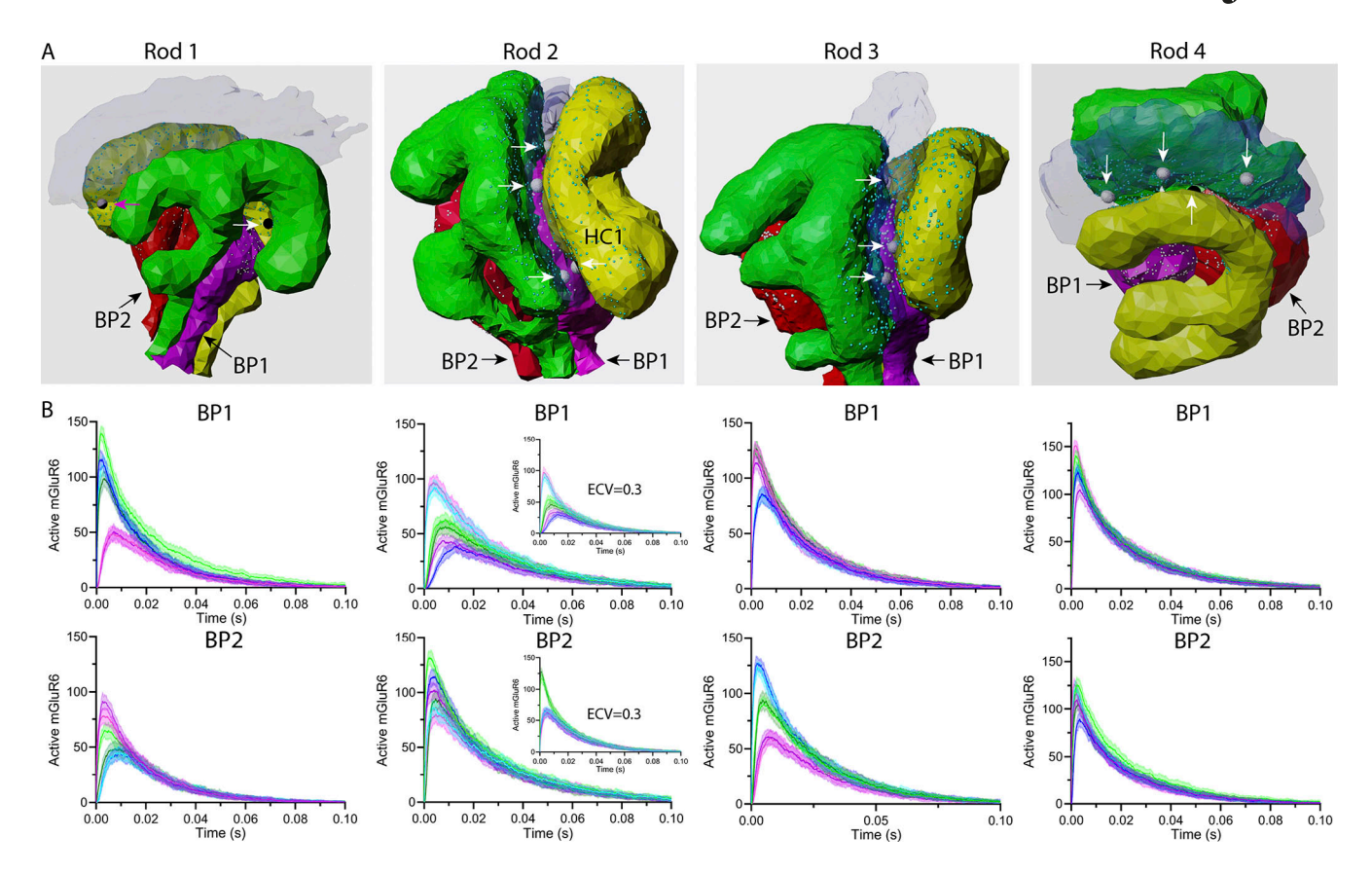


Figure 8. **Differences in the release site location influence mGluR6 activity. (A)** Illustrations of rods 1–4 with their postsynaptic cells. BPs 1 and 2 are shown in magenta (BP1) and red (BP2), respectively. Ribbons are shown in transparent blue. Rod membranes have been removed for easier visualization. Visible release sites are indicated by arrows. The release site corresponding to the magenta trace in BP1 of rod 1 (B) is shown with a magenta arrow. **(B)** Plot of the time course of mGluR6 activated by release at six sites, three on each face of the ribbon. Responses of the two RBPs beneath each rod terminal (BP1 and BP2) are plotted separately. Insets beneath Rod 2 show the effect on mGluR6 activity of increasing the ECV of the synaptic cleft from 0.11 to 0.3. All graphs are the mean ± SD of 25 simulations.

the closing of TRPM1 cation channels via interactions involving α and β/γ G protein subunits (Xu et al., 2016; Shen et al., 2012). Nonlinearities in the cascade could also influence response amplitude and kinetics. RBPs employ a nonlinear thresholding mechanism in which slight changes in glutamate release cause only slight changes in TRPM1 activation, whereas larger changes in release cause disproportionately larger changes in TRPM1 activity (Sampath and Rieke, 2004; Field and Rieke, 2002). This thresholding mechanism filters out small random changes in glutamate release to improve detection of genuine light-evoked changes in release. The threshold for this nonlinearity arises from saturation of the intracellular signaling cascade, which was not included in our model. Our results suggesting that glutamate released from individual vesicles does not saturate mGluR6 are consistent with these previous results. By eliminating smaller events arising from release at more distant ribbon sites, such a nonlinearity might help to reduce quantal variability arising from differences in synaptic geometry and release site location.

AMPARs

We found that model parameters developed to fit AMPARs in hippocampal pyramidal neurons yielded good fits to decay kinetics of single-vesicle mEPSCs in retinal HCs (Jonas et al., 1993). Both types of neurons possess GluA2 receptors (Ströh et al., 2018; Hack et al., 2001). Our simulations predicted a faster rise time than observed in actual mEPSCs, but this could result from limitations in the voltage clamp speed of HCs that are strongly coupled to their neighbors.

Unitary mEPSCs in mouse HCs average 3.5 pA in amplitude (Feigenspan and Babai, 2015) and can be generated by opening only three to five AMPAR channels (Hansen et al., 2021). We achieved a similar number of channel openings per vesicle release event when we placed 200 receptors on each HC dendrite. Comparisons of reconstructed synapses with a sphere model showed that AMPAR kinetics is dominated by intrinsic receptor kinetics, including receptor binding, activation, and desensitization. The low affinity of AMPARs leads to rapid deactivation that is enhanced by rapid receptor desensitization (Hansen et al., 2021). During sustained release from photoreceptors, interevent intervals between mEPSCs in HCs are typically longer than the time required for recovery from AMPAR desensitization (Pang et al., 2008; Feigenspan and Babai, 2015). Thus, AMPAR desensitization helps to keep quanta distinct from one another without impairing the postsynaptic impact of subsequent release events. Kinetic differences among simulated mEPSCs were seen in only a few cases with exceedingly small responses

Journal of General Physiology

15 of 20



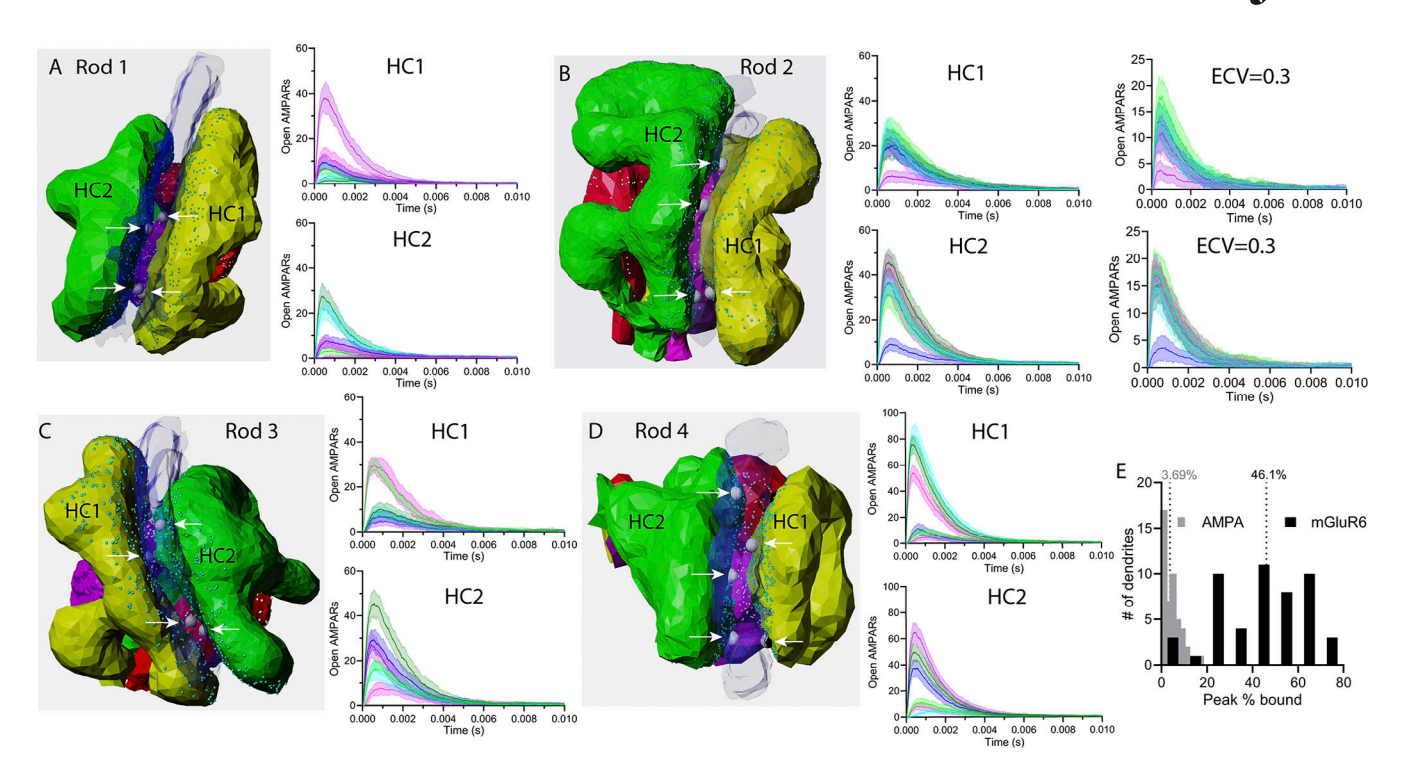


Figure 9. **Differences in the release site location influence AMPAR activity. (A)** Rod 1 along with its postsynaptic partners. HCs 1 and 2 are shown in yellow (HC1) and green (HC2), respectively. Ribbons are in transparent blue. Rod membranes have been removed for easier visualization. Visible release sites are denoted by arrows. Graphs plot time-dependent activation of AMPARs by release at six different sites, three on each face of the ribbon. Responses of the two HCs beneath each rod terminal (HC1 and HC2) are plotted separately. **(B)** Illustration of rod 2 with graphs of AMPAR activity in HC1 and HC2. Site-to-site variability remained after increasing the ECV from 0.11 to 0.3. **(C)** Illustration of rod 3 with graphs of AMPAR activity in HC1 and HC2. **(D)** Illustration of rod 4 with graphs of AMPAR activity in HC1 and HC2. **(E)** Frequency histogram of the peak percentage of activated HC AMPA (gray) and RBP mGluR6 receptors (black) produced by release at different ribbon sites. For these simulations, we increased the number of AMPARs on each HC from 200 to 500. Graphs plot the mean ± SD of 25 simulations.

evoked by release at sites distant from individual HC dendrites. By promoting temporal independence of quanta, rapid deactivation and receptor desensitization promote linear summation of individual events that in turn help to produce relatively linear contrast–response curves in HCs (Burkhardt et al., 2004). This differs from the steep contrast–response curves in most BPs (Burkhardt et al., 2004). By providing a linear readout of rod and cone membrane voltage, these mechanisms promote linear regulation of photoreceptor output via inhibitory feedback from HCs (Thoreson and Mangel, 2012).

EAAT5

Studies by Hasegawa et al. (2006) suggested that presynaptic EAAT5 may retrieve much of the glutamate released by rods. Consistent with a role of this transporter at photoreceptor synapses, genetic elimination of EAAT5 impairs the frequency responses of downstream neurons (Gehlen et al., 2021). The heterologous expression of EAAT5 suggested that uptake by this transporter may be too slow to contribute significantly at rod synapses, but EAAT5 expressed in rods shows fast kinetics suitable for retrieval (Schneider et al., 2014; Thoreson and Chhunchha, 2023). Müller cells whose processes envelope rod terminals (Sarantis and Mobbs, 1992) are also capable of significant glutamate uptake mediated by EAAT1 (Pow et al., 2000; Sarthy et al., 2005). Furthermore, pharmacological inhibition

and genetic elimination of EAAT1 impair ERG b-waves that arise from the actions of photoreceptor glutamate release on BP (Tse et al., 2014; Harada et al., 1998). We used our model to assess the contributions of EAAT5 versus Müller cell uptake. To do so, we adapted an existing model for EAAT2 to describe the kinetics of EAAT5 I_{A(glu)} evoked by single-vesicle release events in rods (Kolen et al., 2020). Based on the amplitude of evoked and single-vesicle I_{A(glu)} events in rods, we concluded that there are ~3,000 EAAT5 at each rod spherule. Following glutamate release, these transporters can rapidly bind up to 3,000 glutamate molecules. Glutamate transport into the rod is slow but nevertheless capable of maintaining glutamate uptake at rates equivalent to 32 vesicles/s. This is close to the peak rate of sustained release by rods of 36 vesicles/s estimated from the size of the readily releasable pool (90 vesicles) and the rate at which that pool can be replenished (2.5/s) (Mesnard et al., 2022a, 2022b; Grabner et al., 2023; Grabner and Moser, 2021).

While EAAT5 may be able to keep up with much of the release in darkness, glutamate levels nevertheless decline much more rapidly when the synapse remains open and Müller cell uptake is present. In this context, the principal role of Müller cells thus appears to be helping to maintain a steep concentration gradient for glutamate at the exit of the synaptic invagination. The high glutamate affinity of EAAT1 (2 μM) in Müller cells is well suited for this role since dilution, along with uptake



by EAAT5, dramatically reduces the concentration of glutamate that exits the cleft. EAAT2 is concentrated in cones but is also found in rods, where it might contribute to glutamate retrieval (Arriza et al., 1997; Eliasof et al., 1998; Gehlen et al., 2021; Tang et al., 2022; Pow and Barnett, 2000). However, genetic elimination and pharmacological inhibition of EAAT2 have only small effects on dark-adapted ERG b-waves (Harada et al., 1998; Tse et al., 2014) suggesting minor contributions to uptake. Pharmacological inhibition of EAAT2 also has no effect on $I_{A(glu)}$ in rods (Thoreson and Chhunchha, 2023). Our results therefore support earlier studies showing that Müller cell uptake retrieves most of the glutamate that exits rod spherules (Eliasof et al., 1998; Rauen et al., 1996, 1998; Barnett and Pow, 2000; Pow et al., 2000; Harada et al., 1998; Sarthy et al., 2005; Fyk-Kolodziej et al., 2004; Derouiche, 1996) but are also consistent with Hasegawa et al. (2006) by showing that binding to EAAT5 speeds glutamate decline in the synaptic invagination.

In addition to controlling glutamate levels in the cleft, $I_{A(glu)}$ activated by glutamate binding to EAAT5 can also modify rod responses directly by altering rod membrane voltage, input resistance, and Ca^{2+} channel activity. The chloride equilibrium potential in rods is approximately -20 mV (Thoreson et al., 2003), and so $I_{A(glu)}$ activity in darkness should have a depolarizing effect on rods. However, the stimulatory effects of depolarization are opposed by direct effects of chloride efflux that reduce the open probability of L-type Ca^{2+} channels via actions at specific anion-binding sites (Rabl et al., 2003; Thoreson et al., 1997, 2000; Babai et al., 2010). This inhibitory effect of chloride efflux helps to limit regenerative activation of Ca^{2+} channels and stabilize membrane potential in rods depolarized in darkness. We did not incorporate these and other presynaptic effects into our model.

Sources of synaptic variability

The earlier conclusion that glutamate diffused rapidly through the invaginating synapse also suggested that it equilibrated rapidly throughout the cleft and that postsynaptic dendrites of RBP and HC dendrites all experienced similar glutamate transients in response to individual release events (Rao-Mirotznik et al., 1998). However, our evidence that glutamate exits the invaginating rod synapse more slowly suggests otherwise. Rodto-rod differences in synaptic architecture led to distinct levels of synaptic activity at both RBPs and HCs. We also observed differences within individual rods in the activity of postsynaptic receptors on RBP and HC dendrites. This variability arises from the fact that given the same number of glutamate receptors, a more distant RBP or HC will exhibit a smaller response. We also saw differences in response amplitude in individual RBPs or HCs as a function of release site location. Depending on the anatomical arrangement, release at different sites along a ribbon can sometimes produce large differences in mGluR6 or AMPAR activity in the same postsynaptic cell. The lower affinity of AMPARs made them even more sensitive to differences in release site location than mGluR6. We distributed receptors widely over the tips of RBP and HC dendrites for our simulations. Confining receptor distribution to smaller regions would be expected to produce even more pronounced effects of release site location on receptor activity.

While we saw that mGluR6 and AMPAR activity varied with release site location, differences in release site location did not significantly affect the number of EAAT5 anion channel openings. This suggests that much of the variability in single-vesicle $I_{A(glu)}$ events in rods arises from variability in the amount of glutamate contained within vesicles. Consistent with this, the range of volumes predicted from vesicle diameters measured in electron micrographs (Fuchs et al., 2014) yields coefficients of variation ranging from 0.28 to 0.44, close to the average c.v. for single-vesicle $I_{A(glu)}$ events (0.39) (Thoreson and Chhunchha, 2023). This further implies that much of the variation in the number of molecules per vesicle is explained by variations in diameter, implying that each vesicle contains a similar concentration of glutamate.

Other invaginating synapses

Many other vertebrate and invertebrate neurons make invaginating synapses, which are particularly abundant in Drosophila (Petralia et al., 2021). However, the invaginating spines and calyceal synapses in other regions of the mammalian brain have a simpler architecture that likely limits the effects of geometric tortuosity. At the other end of the spectrum, invaginating synapses of cone photoreceptor cells have an even more complex postsynaptic structure than rods (Sterling and Matthews, 2005) with more than a dozen types of BPs contacting the cone terminal at different sites (Euler et al., 2014). Furthermore, HCs beneath cone terminals have glutamate receptors at both dendrites within the invaginating synapse and on primary dendrites >1 µm away from ribbon release sites (Haverkamp et al., 2000). The complex architecture of cone synapses helps to shape response kinetics, with nearby BP contacts experiencing rapid glutamate changes and distant BP contacts experiencing slower, smoother fluctuations (DeVries et al., 2006). Along with glutamate receptor properties, the unique architecture of this synapse plays a significant role in the initial filtering and segregation of visual responses into different functionally specialized, parallel BP pathways (Grabner et al., 2023).

Implications for rod release rates and detection of dim light by RBPs

The persistence of glutamate in the invaginating synapse allows greater integration between synaptic vesicle release events. For RBPs, our simulations suggest that mGluR6 receptors may remain active for >100 ms after the release of a single vesicle. Rao et al. (1994) suggested that release from rods in darkness must be fast enough so that release events are consistently separated by time intervals shorter than a single-vesicle response. Given that single-vesicle events last >100 ms and assuming Poisson rates of release, this constraint can be achieved with rates of <25 quanta/ s. However, Rao-Mirotznik et al. (1998) noted that release must also be fast enough to minimize the possibility that a random interval might be mistaken for a genuine slowing of release produced by capture of a single photon. They concluded this required release rates of 100 vesicles/s or more. This exceeds the upper limit on rod release rates of 36 vesicles/s placed by the size of the readily releasable pool and the rate at which that pool can be replenished (Grabner et al., 2023). One possible solution



to this apparent dilemma is that release may occur at more regular intervals than predicted by the Poisson statistics, thus allowing detection at lower release rates (Schein and Ahmad, 2005). Consistent with this possibility, measurements from rods held at the typical membrane potential in darkness of -40 mV suggest that they release vesicles in multivesicular bursts at regular intervals (Hays et al., 2020, 2021).

Each RBP receives synaptic input from an average of 25 rods (Tsukamoto and Omi, 2013; Tsukamoto et al., 2001). When detecting a single photon event, RBPs must distinguish a small reduction in glutamate release occurring in only one of these 25 rods. Our results suggest several additional sources of synaptic variability that may complicate this already challenging task. These include differences in rod inputs arising from differences in vesicular glutamate content, geometric tortuosity of rod synapses, anatomy of RBP dendrites, location of release sites along the ribbon, location of mGluR6 receptors, and the numbers of receptors. How are single photon responses extracted from noise in the face of this variability? In addition to the possibility of regular release, RBPs employ a nonlinear thresholding mechanism to extract larger single photon responses from noise (Field and Rieke, 2002; Sampath and Rieke, 2004). It is also possible that retinas will compensate during development for different input strengths by adjusting receptor numbers and/or location to ensure that all the inputs into an RBP are similar. Detailed models of rod spherules offer an opportunity to explore the limitations of these and other potential mechanisms that might be employed for detection of single photon responses by RBPs.

Our simulations revealed surprisingly slow glutamate kinetics at invaginating rod synapses. Slow kinetics allows greater integration of release events at RBP synapses that in turn allows lower release rates to sustain postsynaptic activity in darkness. However, the slow kinetics of glutamate removal introduces additional potential sources of quantal variability by exposing different dendrites to different changes in glutamate. The mechanisms employed by rods to overcome these and other sources of quantal variability and detect light-evoked changes in glutamate release remain to be explored fully.

Data availability

Serial block-face electron micrographs of the outer mouse retina used for reconstructions are available as TIF files on the Synapse Data Repository (https://www.synapse.org/Synapse:syn64720975). Acquisition details for these files are described at https://www.synapse.org/Synapse:syn64720933. MCell4 models of the four rods used in this study are posted at Mcell.org (http://www.mcell.cnl.salk.edu/models/rod-synapses-2025-1). Serial block-face scanning electron micrographs of mouse outer retina data is also accessable at https://doi.org/10.5061/dryad.tb2rbp0cq.

Acknowledgments

Jeanne M. Nerbonne served as editor.

The authors thank Johann Pahlberg (National Eye Institute) for permission to use his unpublished data concerning the kinetics of RBP light responses. The authors would also like to thank Tom Bargar of the Electron Microscopy Core Facility

(EMCF) at the University of Nebraska Medical Center for technical assistance.

This work was supported by the National Institute of Neurological Disorders and Stroke Intramural Research Program (NS003039 to J.S. Diamond), National Institutes of Health (NIH) EY10542 (to W.B. Thoreson), NIH EY32396 (to W.B. Thoreson), NIH MMBioS P41-GM103712 (to T.M. Bartol), NIH CRCNS R01-MH115556 (to T.M. Bartol), NIH CRCNS R01-MH129066 (to T.M. Bartol), National Science Foundation (NSF) NeuroNex DBI-1707356 (to T.M. Bartol), and NSF NeuroNex DBI-2014862 (to T.M. Bartol). The EMCF is supported by the NIH grant 1S10OD026790-01, state funds from the Nebraska Research Initiative, the University of Nebraska Foundation, and institutionally the Office of the Vice Chancellor for Research. This work was completed utilizing the Holland Computing Center of the University of Nebraska, which receives support from the UNL Office of Research and Economic Development, and the Nebraska Research Initiative.

Author contributions: W.B. Thoreson: conceptualization, formal analysis, investigation, software, visualization, and writing—original draft. T.M. Bartol: conceptualization, data curation, formal analysis, funding acquisition, investigation, methodology, resources, software, validation, visualization, and writing—original draft, review, and editing. N.H. Conoan: data curation, resources, and writing—review and editing. J.S. Diamond: conceptualization, methodology, project administration, supervision, and writing—original draft, review, and editing.

Disclosures: N.H. Conoan reported owning a small portion of stock (approximately 10 shares) in Thermo Fisher Scientific, the manufacturer of the instrument used to collect the Serial Block Face Imaging data. No other disclosures were reported.

Submitted: 16 December 2024 Revised: 24 January 2025 Accepted: 5 February 2025

References

Arriza, J.L., S. Eliasof, M.P. Kavanaugh, and S.G. Amara. 1997. Excitatory amino acid transporter 5, a retinal glutamate transporter coupled to a chloride conductance. Proc. Natl. Acad. Sci. USA. 94:4155–4160. https:// doi.org/10.1073/pnas.94.8.4155

Attwell, D., M. Sarantis, B. Barbour, and H. Brew. 1989. Electrogenic glutamate uptake in amphibian and mammalian retinal glial cells. Acta Physiol. Scand. Suppl. 582:44.

Babai, N., N. Kanevsky, N. Dascal, G.J. Rozanski, D.P. Singh, N. Fatma, and W.B. Thoreson. 2010. Anion-sensitive regions of L-type CaV1.2 calcium channels expressed in HEK293 cells. PLoS One. 5:e8602. https://doi.org/ 10.1371/journal.pone.0008602

Barnett, N.L., and D.V. Pow. 2000. Antisense knockdown of GLAST, a glial glutamate transporter, compromises retinal function. *Invest. Oph-thalmol. Vis. Sci.* 41:585–591.

Bartol, T.M., D.X. Keller, J.P. Kinney, C.L. Bajaj, K.M. Harris, T.J. Sejnowski, and M.B. Kennedy. 2015. Computational reconstitution of spine calcium transients from individual proteins. Front. Synaptic Neurosci. 7:17. https://doi.org/10.3389/fnsyn.2015.00017

Berntson, A., R.G. Smith, and W.R. Taylor. 2004. Transmission of single photon signals through a binary synapse in the mammalian retina. Vis. Neurosci. 21:693–702. https://doi.org/10.1017/S0952523804215048

Burkhardt, D.A., P.K. Fahey, and M.A. Sikora. 2004. Retinal bipolar cells: Contrast encoding for sinusoidal modulation and steps of



- luminance contrast. Vis. Neurosci. 21:883-893. https://doi.org/10.1017/S095252380421608X
- Cadetti, L., T.M. Bartoletti, and W.B. Thoreson. 2008. Quantal mEPSCs and residual glutamate: How horizontal cell responses are shaped at the photoreceptor ribbon synapse. Eur. J. Neurosci. 27:2575–2586. https:// doi.org/10.1111/j.1460-9568.2008.06226.x
- Derouiche, A. 1996. Possible role of the Müller cell in uptake and metabolism of glutamate in the mammalian outer retina. Vis. Res. 36:3875–3878. https://doi.org/10.1016/S0042-6989(96)00140-X
- DeVries, S.H., W. Li, and S. Saszik. 2006. Parallel processing in two transmitter microenvironments at the cone photoreceptor synapse. *Neuron*. 50:735-748. https://doi.org/10.1016/j.neuron.2006.04.034
- Eliasof, S., J.L. Arriza, B.H. Leighton, M.P. Kavanaugh, and S.G. Amara. 1998. Excitatory amino acid transporters of the salamander retina: Identification, localization, and function. *J. Neurosci.* 18:698–712. https://doi.org/10.1523/INEUROSCI.18-02-00698.1998
- Eliasof, S., and C.E. Jahr. 1996. Retinal glial cell glutamate transporter is coupled to an anionic conductance. *Proc. Natl. Acad. Sci. USA*. 93: 4153–4158. https://doi.org/10.1073/pnas.93.9.4153
- Euler, T., S. Haverkamp, T. Schubert, and T. Baden. 2014. Retinal bipolar cells: Elementary building blocks of vision. Nat. Rev. Neurosci. 15: 507-519. https://doi.org/10.1038/nrn3783
- Feigenspan, A., and N. Babai. 2015. Functional properties of spontaneous excitatory currents and encoding of light/dark transitions in horizontal cells of the mouse retina. Eur. J. Neurosci. 42:2615–2632. https://doi.org/ 10.1111/ein.13016
- Feigenspan, A., and N.Z. Babai. 2017. Preparation of horizontal slices of adult mouse retina for electrophysiological studies. J. Vis. Exp. 119:55173. https://doi.org/10.3791/55173-v
- Field, G.D., and F. Rieke. 2002. Nonlinear signal transfer from mouse rods to bipolar cells and implications for visual sensitivity. *Neuron.* 34:773–785. https://doi.org/10.1016/S0896-6273(02)00700-6
- Franks, K.M., T.M. Bartol. Jr., and T.J. Sejnowski. 2002. A Monte Carlo model reveals independent signaling at central glutamatergic synapses. Biophys. J. 83:2333–2348. https://doi.org/10.1016/S0006-3495(02)75248-X
- Fuchs, M., J.H. Brandstätter, and H. Regus-Leidig. 2014. Evidence for a Clathrin-independent mode of endocytosis at a continuously active sensory synapse. Front. Cell. Neurosci. 8:60. https://doi.org/10.3389/ fncel.2014.00060
- Fyk-Kolodziej, B., P. Qin, A. Dzhagaryan, and R.G. Pourcho. 2004. Differential cellular and subcellular distribution of glutamate transporters in the cat retina. Vis. Neurosci. 21:551–565. https://doi.org/10.1017/S0952523804214067
- Garcia, J.W., T.M. Bartol, and T.J. Sejnowski. 2022. Multiscale modeling of presynaptic dynamics from molecular to mesoscale. PLoS Comput. Biol. 18:e1010068. https://doi.org/10.1371/journal.pcbi.1010068
- Gehlen, J., Aretzweiler, C., Mataruga, A., Fahlke, C. and Muller, F. 2021. Excitatory amino acid transporter EAAT5 improves temporal resolution in the retina. eNeuro. 8:ENEURO.0406-21.2021. https://doi.org/10.1523/ENEURO.0406-21.2021
- Grabner, C.P., D. Futagi, J. Shi, V. Bindokas, K. Kitano, E.A. Schwartz, and S.H. DeVries. 2023. Mechanisms of simultaneous linear and nonlinear computations at the mammalian cone photoreceptor synapse. *Nat. Commun.* 14:3486. https://doi.org/10.1038/s41467-023-38943-2
- Grabner, C.P., and T. Moser. 2021. The mammalian rod synaptic ribbon is essential for Ca_v channel facilitation and ultrafast synaptic vesicle fusion. Elife. 10:e63844. https://doi.org/10.7554/eLife.63844
- Grant, G.B., and F.S. Werblin. 1996. A glutamate-elicited chloride current with transporter-like properties in rod photoreceptors of the tiger salamander. Vis. Neurosci. 13:135–144. https://doi.org/10.1017/S0952523800007185
- Grassmeyer, J.J., and W.B. Thoreson. 2017. Synaptic ribbon active zones in cone photoreceptors operate independently from one another. *Front. Cell. Neurosci.* 11:198. https://doi.org/10.3389/fncel.2017.00198
- Grosskreutz, J., A. Zoerner, F. Schlesinger, K. Krampfl, R. Dengler, and J. Bufler. 2003. Kinetic properties of human AMPA-type glutamate receptors expressed in HEK293 cells. Eur. J. Neurosci. 17:1173–1178. https://doi.org/10.1046/j.1460-9568.2003.02531.x
- Hack, I., M. Frech, O. Dick, L. Peichl, and J.H. Brandstätter. 2001. Heterogeneous distribution of AMPA glutamate receptor subunits at the photoreceptor synapses of rodent retina. Eur. J. Neurosci. 13:15–24. https://doi.org/10.1111/j.1460-9568.2001.01357.x
- Haeseleer, F., B. Williams, and A. Lee. 2016. Characterization of C-terminal splice variants of Cav1.4 Ca2+ channels in human retina. J. Biol. Chem. 291:15663–15673. https://doi.org/10.1074/jbc.M116.731737

- Hansen, K.B., L.P. Wollmuth, D. Bowie, H. Furukawa, F.S. Menniti, A.I. Sobolevsky, G.T. Swanson, S.A. Swanger, I.H. Greger, T. Nakagawa, et al. 2021. Structure, function, and pharmacology of glutamate receptor ion channels. *Pharmacol. Rev.* 73:298–487. https://doi.org/10.1124/pharmrev.120.000131
- Harada, T., C. Harada, M. Watanabe, Y. Inoue, T. Sakagawa, N. Nakayama, S. Sasaki, S. Okuyama, K. Watase, K. Wada, and K. Tanaka. 1998. Functions of the two glutamate transporters GLAST and GLT-1 in the retina. Proc. Natl. Acad. Sci. USA. 95:4663–4666. https://doi.org/10.1073/pnas.95.8.4663
- Hasegawa, J., T. Obara, K. Tanaka, and M. Tachibana. 2006. High-density presynaptic transporters are required for glutamate removal from the first visual synapse. *Neuron*. 50:63-74. https://doi.org/10.1016/j.neuron .2006.02.022
- Haverkamp, S., U. Grünert, and H. Wässle. 2000. The cone pedicle, a complex synapse in the retina. *Neuron*. 27:85–95. https://doi.org/10.1016/S0896-6273(00)00011-8
- Hays, C.L., A.L. Sladek, G.D. Field, and W.B. Thoreson. 2021. Properties of multivesicular release from mouse rod photoreceptors support transmission of single-photon responses. *Elife*. 10:e67446. https://doi.org/10 .7554/eLife.67446
- Hays, C.L., A.L. Sladek, and W.B. Thoreson. 2020. Resting and stimulated mouse rod photoreceptors show distinct patterns of vesicle release at ribbon synapses. J. Gen. Physiol. 152:e202012716. https://doi.org/10 .1085/jgp.202012716
- Husar, A., M. Ordyan, G.C. Garcia, J.G. Yancey, A.S. Saglam, J.R. Faeder, T.M. Bartol, M.B. Kennedy, and T.J. Sejnowski. 2024. MCell4 with BioNet-Gen: A Monte Carlo simulator of rule-based reaction-diffusion systems with Python interface. PLoS Comput. Biol. 20:e1011800. https://doi.org/10.1371/journal.pcbi.1011800
- Husar, A., M. Ordyan, G.C. Garcia, J.G. Yancey, A.S. Saglam, J.R. Faeder, T.M. Bartol, and T.J. Sejnowski. 2022. MCell4 with BioNetGen: A Monte Carlo simulator of rule-based reaction-diffusion systems with Python interface. bioRxiv. https://doi.org/10.1101/2022.05.17.492333 (Preprint post May 01, 2023).
- Jonas, P., G. Major, and B. Sakmann. 1993. Quantal components of unitary EPSCs at the mossy fibre synapse on CA3 pyramidal cells of rat hippocampus. J. Physiol. 472:615-663. https://doi.org/10.1113/jphysiol.1993 sp019965
- Kerr, R.A., T.M. Bartol, B. Kaminsky, M. Dittrich, J.C. Chang, S.B. Baden, T.J. Sejnowski, and J.R. Stiles. 2008. Fast Monte Carlo simulation methods for biological reaction-diffusion systems in solution and on surfaces. SIAM J. Sci. Comput. 30:3126–3149. https://doi.org/10.1137/070692017
- Kim, H.G., and R.F. Miller. 1993. Properties of synaptic transmission from photoreceptors to bipolar cells in the mudpuppy retina. J. Neurophysiol. 69:352-360. https://doi.org/10.1152/jn.1993.69.2.352
- Koike, C., T. Numata, H. Ueda, Y. Mori, and T. Furukawa. 2010a. TRPMI: A vertebrate TRP channel responsible for retinal ON bipolar function. Cell Calcium. 48:95–101. https://doi.org/10.1016/j.ceca.2010.08.004
- Koike, C., T. Obara, Y. Uriu, T. Numata, R. Sanuki, K. Miyata, T. Koyasu, S. Ueno, K. Funabiki, A. Tani, et al. 2010b. TRPM1 is a component of the retinal ON bipolar cell transduction channel in the mGluR6 cascade. Proc. Natl. Acad. Sci. USA. 107:332–337. https://doi.org/10.1073/pnas.0912730107
- Kolen, B., D. Kortzak, A. Franzen, and C. Fahlke. 2020. An amino-terminal point mutation increases EAAT2 anion currents without affecting glutamate transport rates. J. Biol. Chem. 295:14936-14947. https://doi.org/10.1074/jbc.RA120.013704
- Larsson, H.P., S.A. Picaud, F.S. Werblin, and H. Lecar. 1996. Noise analysis of the glutamate-activated current in photoreceptors. *Biophys. J.* 70: 733-742. https://doi.org/10.1016/S0006-3495(96)79613-3
- Levitz, J., C. Habrian, S. Bharill, Z. Fu, R. Vafabakhsh, and E.Y. Isacoff. 2016. Mechanism of assembly and cooperativity of homomeric and heteromeric metabotropic glutamate receptors. *Neuron.* 92:143–159. https://doi.org/10.1016/j.neuron.2016.08.036
- Lu, W., Y. Shi, A.C. Jackson, K. Bjorgan, M.J. During, R. Sprengel, P.H. Seeburg, and R.A. Nicoll. 2009. Subunit composition of synaptic AMPA receptors revealed by a single-cell genetic approach. *Neuron.* 62: 254–268. https://doi.org/10.1016/j.neuron.2009.02.027
- Machtens, J.P., D. Kortzak, C. Lansche, A. Leinenweber, P. Kilian, B. Begemann, U. Zachariae, D. Ewers, B.L. de Groot, R. Briones, and C. Fahlke. 2015. Mechanisms of anion conduction by coupled glutamate transporters. Cell. 160:542–553. https://doi.org/10.1016/j.cell.2014.12.035
- Mesnard, C.S., C.L. Barta, A.L. Sladek, D. Zenisek, and W.B. Thoreson. 2022a. Eliminating synaptic ribbons from rods and cones halves the releasable



- vesicle pool and slows down replenishment. *Int. J. Mol. Sci.* 23:6429. https://doi.org/10.3390/ijms23126429
- Mesnard, C.S., C.L. Hays, C.L. Barta, A.L. Sladek, J.J. Grassmeyer, K.K. Hinz, R.M. Quadros, C.B. Gurumurthy, and W.B. Thoreson. 2022b. Synaptotagmins 1 and 7 in vesicle release from rods of mouse retina. *Exp. Eye* Res. 225:109279. https://doi.org/10.1016/j.exer.2022.109279
- Migdale, K., S. Herr, K. Klug, K. Ahmad, K. Linberg, P. Sterling, and S. Schein. 2003. Two ribbon synaptic units in rod photoreceptors of macaque, human, and cat. J. Comp. Neurol. 455:100–112. https://doi.org/10.1002/cne.10501
- Morgans, C.W., R.L. Brown, and R.M. Duvoisin. 2010. TRPM1: The endpoint of the mGluR6 signal transduction cascade in retinal ON-bipolar cells. *BioEssays*. 32:609–614. https://doi.org/10.1002/bies.200900198
- Moser, T., C.P. Grabner, and F. Schmitz. 2020. Sensory processing at ribbon synapses in the retina and the cochlea. *Physiol. Rev.* 100:103–144. https://doi.org/10.1152/physrev.00026.2018
- Nicholson, C., and S. Hrabětová. 2017. Brain extracellular space: The final frontier of neuroscience. *Biophys. J.* 113:2133–2142. https://doi.org/10.1016/j.bpj.2017.06.052
- Nicholson, C., J.M. Phillips, and A.R. Gardner-Medwin. 1979. Diffusion from an iontophoretic point source in the brain: Role of tortuosity and volume fraction. *Brain Res.* 169:580–584. https://doi.org/10.1016/0006-8993(79)90408-6
- Nielsen, T.A., D.A. DiGregorio, and R.A. Silver. 2004. Modulation of glutamate mobility reveals the mechanism underlying slow-rising AMPAR EPSCs and the diffusion coefficient in the synaptic cleft. *Neuron.* 42: 757–771. https://doi.org/10.1016/j.neuron.2004.04.003
- Niklaus, S., L. Cadetti, C.M. Vom Berg-Maurer, A. Lehnherr, A.L. Hotz, I.C. Forster, M. Gesemann, and S.C.F. Neuhauss. 2017. Shaping of signal transmission at the photoreceptor synapse by EAAT2 glutamate transporters. eNeuro. 4: ENEURO.0339-16.2017. https://doi.org/10.1523/ENEURO.0339-16.2017
- Nomura, A., R. Shigemoto, Y. Nakamura, N. Okamoto, N. Mizuno, and S. Nakanishi. 1994. Developmentally regulated postsynaptic localization of a metabotropic glutamate receptor in rat rod bipolar cells. Cell. 77: 361–369. https://doi.org/10.1016/0092-8674(94)90151-1
- Orrego, F., and S. Villanueva. 1993. The chemical nature of the main central excitatory transmitter: A critical appraisal based upon release studies and synaptic vesicle localization. *Neuroscience*. 56:539–555. https://doi.org/10.1016/0306-4522(93)90355-J
- Pang, J.J., F. Gao, A. Barrow, R.A. Jacoby, and S.M. Wu. 2008. How do tonic glutamatergic synapses evade receptor desensitization? J. Physiol. 586: 2889–2902. https://doi.org/10.1113/jphysiol.2008.151050
- Petralia, R.S., P.J. Yao, D. Kapogiannis, and Y.X. Wang. 2021. Invaginating structures in synapses perspective. Front. Synaptic Neurosci. 13:685052. https://doi.org/10.3389/fnsyn.2021.685052
- Pin, J.P., and F. Acher. 2002. The metabotropic glutamate receptors: Structure, activation mechanism and pharmacology. *Curr. Drug Targets CNS Neurol. Disord.* 1:297–317. https://doi.org/10.2174/1568007023339328
- Pin, J.P., and B. Bettler. 2016. Organization and functions of mGlu and GABA_B receptor complexes. *Nature*. 540:60-68. https://doi.org/10 .1038/nature20566
- Pow, D.V., and N.L. Barnett. 2000. Developmental expression of excitatory amino acid transporter 5: A photoreceptor and bipolar cell glutamate transporter in rat retina. *Neurosci. Lett.* 280:21–24. https://doi.org/10.1016/S0304-3940(99)00988-X
- Pow, D.V., N.L. Barnett, and P. Penfold. 2000. Are neuronal transporters relevant in retinal glutamate homeostasis? *Neurochem. Int.* 37:191–198. https://doi.org/10.1016/S0197-0186(00)00022-X
- Rabl, K., E.J. Bryson, and W.B. Thoreson. 2003. Activation of glutamate transporters in rods inhibits presynaptic calcium currents. Vis. Neurosci. 20:557-566. https://doi.org/10.1017/S0952523803205095
- Rao-Mirotznik, R., G. Buchsbaum, and P. Sterling. 1998. Transmitter concentration at a three-dimensional synapse. J. Neurophysiol. 80: 3163–3172. https://doi.org/10.1152/jn.1998.80.6.3163
- Rao-Mirotznik, R., A.B. Harkins, G. Buchsbaum, and P. Sterling. 1995. Mammalian rod terminal: Architecture of a binary synapse. *Neuron*. 14: 561–569. https://doi.org/10.1016/0896-6273(95)90312-7
- Rao, R., G. Buchsbaum, and P. Sterling. 1994. Rate of quantal transmitter release at the mammalian rod synapse. *Biophys. J.* 67:57–63. https://doi.org/10.1016/S0006-3495(94)80454-0
- Rauen, T., J.D. Rothstein, and H. Wässle. 1996. Differential expression of three glutamate transporter subtypes in the rat retina. Cell Tissue Res. 286: 325-336. https://doi.org/10.1007/s004410050702
- Rauen, T., W.R. Taylor, K. Kuhlbrodt, and M. Wiessner. 1998. High-affinity glutamate transporters in the rat retina: A major role of the glial

- glutamate transporter GLAST-1 in transmitter clearance. *Cell Tissue Res.* 291:19–31. https://doi.org/10.1007/s004410050976
- Riveros, N., J. Fiedler, N. Lagos, C. Muñoz, and F. Orrego. 1986. Glutamate in rat brain cortex synaptic vesicles: Influence of the vesicle isolation procedure. *Brain Res.* 386:405-408. https://doi.org/10.1016/0006-8993(86)90181-2
- Rusakov, D.A., and D.M. Kullmann. 1998. Geometric and viscous components of the tortuosity of the extracellular space in the brain. *Proc. Natl. Acad. Sci. USA*. 95:8975–8980. https://doi.org/10.1073/pnas.95.15.8975
- Saha, A., J. Zuniga, K. Mian, H. Zhai, P.J. Derr, M. Hoon, and R. Sinha. 2023. Regional variation in the organization and connectivity of the first synapse in the primate night vision pathway. iScience. 26:108113. https://doi.org/10.1016/j.isci.2023.108113
- Sampath, A.P., and F. Rieke. 2004. Selective transmission of single photon responses by saturation at the rod-to-rod bipolar synapse. Neuron. 41: 431-443. https://doi.org/10.1016/S0896-6273(04)00005-4
- Sarantis, M., and P. Mobbs. 1992. The spatial relationship between Müller cell processes and the photoreceptor output synapse. Brain Res. 584: 299-304. https://doi.org/10.1016/0006-8993(92)90909-S
- Sarthy, V.P., L. Pignataro, T. Pannicke, M. Weick, A. Reichenbach, T. Harada, K. Tanaka, and R. Marc. 2005. Glutamate transport by retinal Muller cells in glutamate/aspartate transporter-knockout mice. Glia. 49: 184–196. https://doi.org/10.1002/glia.20097
- Schein, S., and K.M. Ahmad. 2005. A clockwork hypothesis: Synaptic release by rod photoreceptors must be regular. Biophys. J. 89:3931-3949. https://doi.org/10.1529/biophysj.105.070623
- Schneider, F.M., F. Mohr, M. Behrendt, and J. Oberwinkler. 2015. Properties and functions of TRPM1 channels in the dendritic tips of retinal ONbipolar cells. Eur. J. Cell Biol. 94:420–427. https://doi.org/10.1016/j.ejcb .2015.06.005
- Schneider, N., S. Cordeiro, J.P. Machtens, S. Braams, T. Rauen, and C. Fahlke.
 2014. Functional properties of the retinal glutamate transporters GLT-1c
 and EAAT5. J. Biol. Chem. 289:1815–1824. https://doi.org/10.1074/jbc
- Shen, Y., M.A. Rampino, R.C. Carroll, and S. Nawy. 2012. G-protein-mediated inhibition of the Trp channel TRPM1 requires the Gβγ dimer. *Proc. Natl. Acad. Sci. USA*. 109:8752–8757. https://doi.org/10.1073/pnas.1117433109
- Sterling, P., and G. Matthews. 2005. Structure and function of ribbon synapses. Trends Neurosci. 28:20–29. https://doi.org/10.1016/j.tins.2004.11.009
- Stiles, J.R., D. Van Helden, T.M. Bartol Jr., E.E. Salpeter, and M.M. Salpeter. 1996. Miniature endplate current rise times less than 100 microseconds from improved dual recordings can be modeled with passive acetylcholine diffusion from a synaptic vesicle. *Proc. Natl. Acad. Sci. USA*. 93: 5747–5752. https://doi.org/10.1073/pnas.93.12.5747
- Ströh, S., C. Puller, S. Swirski, M.B. Hölzel, L.I.S. van der Linde, J. Segelken, K. Schultz, C. Block, H. Monyer, K. Willecke, et al. 2018. Eliminating glutamatergic input onto horizontal cells changes the dynamic range and receptive Field organization of mouse retinal ganglion cells. J. Neurosci. 38:2015–2028. https://doi.org/10.1523/JNEUROSCI.0141-17.2018
- Syková, E. 2004. Diffusion properties of the brain in health and disease.

 Neurochem. Int. 45:453-466. https://doi.org/10.1016/j.neuint.2003.11
 .009
- Szmajda, B.A., and S.H. Devries. 2011. Glutamate spillover between mammalian cone photoreceptors. *J. Neurosci.* 31:13431–13441. https://doi.org/10.1523/JNEUROSCI.2105-11.2011
- Takamori, S., M. Holt, K. Stenius, E.A. Lemke, M. Grønborg, D. Riedel, H. Urlaub, S. Schenck, B. Brügger, P. Ringler, et al. 2006. Molecular anatomy of a trafficking organelle. Cell. 127:831–846. https://doi.org/10.1016/j.cell.2006.10.030
- Tang, F.S., H.L. Yuan, J.B. Liu, G. Zhang, S.Y. Chen, and J.B. Ke. 2022. Glu-tamate transporters EAAT2 and EAAT5 differentially shape synaptic transmission from rod bipolar cell terminals. eNeuro. 9:ENEURO.0074-22.2022. https://doi.org/10.1523/ENEURO.0074-22.2022
- Thoreson, W.B. 2021. Transmission at rod and cone ribbon synapses in the retina. *Pflugers Arch.* 473:1469–1491. https://doi.org/10.1007/s00424-021-02548-9
- Thoreson, W.B., E.J. Bryson, and K. Rabl. 2003. Reciprocal interactions between calcium and chloride in rod photoreceptors. J. Neurophysiol. 90: 1747–1753. https://doi.org/10.1152/jn.00932.2002
- Thoreson, W.B., and B. Chhunchha. 2023. EAAT5 glutamate transporter rapidly binds glutamate with micromolar affinity in mouse rods. J. Gen. Physiol. 155:155. https://doi.org/10.1085/jgp.202313349
- Thoreson, W.B., and S.C. Mangel. 2012. Lateral interactions in the outer retina. *Prog. Retin. Eye Res.* 31:407-441. https://doi.org/10.1016/j.preteyeres.2012.04.003



- Thoreson, W.B., R. Nitzan, and R.F. Miller. 1997. Reducing extracellular Cl-suppresses dihydropyridine-sensitive Ca2+ currents and synaptic transmission in amphibian photoreceptors. *J. Neurophysiol.* 77:2175–2190. https://doi.org/10.1152/jn.1997.77.4.2175
- Thoreson, W.B., R. Nitzan, and R.F. Miller. 2000. Chloride efflux inhibits single calcium channel open probability in vertebrate photoreceptors: Chloride imaging and cell-attached patch-clamp recordings. Vis. Neurosci. 17:197–206. https://doi.org/10.1017/S0952523800172025
- Thoreson, W.B., K. Rabl, E. Townes-Anderson, and R. Heidelberger. 2004. A highly Ca2+-sensitive pool of vesicles contributes to linearity at the rod photoreceptor ribbon synapse. *Neuron.* 42:595–605. https://doi.org/10.1016/S0896-6273(04)00254-5
- Tse, D.Y., I. Chung, and S.M. Wu. 2014. Pharmacological inhibitions of glutamate transporters EAAT1 and EAAT2 compromise glutamate transport in photoreceptor to ON-bipolar cell synapses. Vis. Res. 103:49–62. https://doi.org/10.1016/j.visres.2014.07.020

- Tsukamoto, Y., K. Morigiwa, M. Ueda, and P. Sterling. 2001. Microcircuits for night vision in mouse retina. *J. Neurosci.* 21:8616–8623. https://doi.org/10.1523/INEUROSCI.21-21-08616.2001
- Tsukamoto, Y., and N. Omi. 2013. Functional allocation of synaptic contacts in microcircuits from rods via rod bipolar to AII amacrine cells in the mouse retina. J. Comp. Neurol. 521:3541–3555. https://doi.org/10.1002/cne.23370
- Tsukamoto, Y., and N. Omi. 2022. Multiple invagination patterns and synaptic efficacy in primate and mouse rod synaptic terminals. *Invest. Ophthalmol. Vis. Sci.* 63:11. https://doi.org/10.1167/iovs.63.8.11
- Wang, Y., H. Fathali, D. Mishra, T. Olsson, J.D. Keighron, K.P. Skibicka, and A.S. Cans. 2019. Counting the number of glutamate molecules in single synaptic vesicles. J. Am. Chem. Soc. 141:17507–17511. https://doi.org/10.1021/jacs.9b09414
- Xu, Y., C. Orlandi, Y. Cao, S. Yang, C.I. Choi, V. Pagadala, L. Birnbaumer, K.A. Martemyanov, and N. Vardi. 2016. The TRPM1 channel in ON-bipolar cells is gated by both the α and the $\beta\gamma$ subunits of the G-protein Go. Sci. Rep. 6:20940. https://doi.org/10.1038/srep20940



Supplemental material

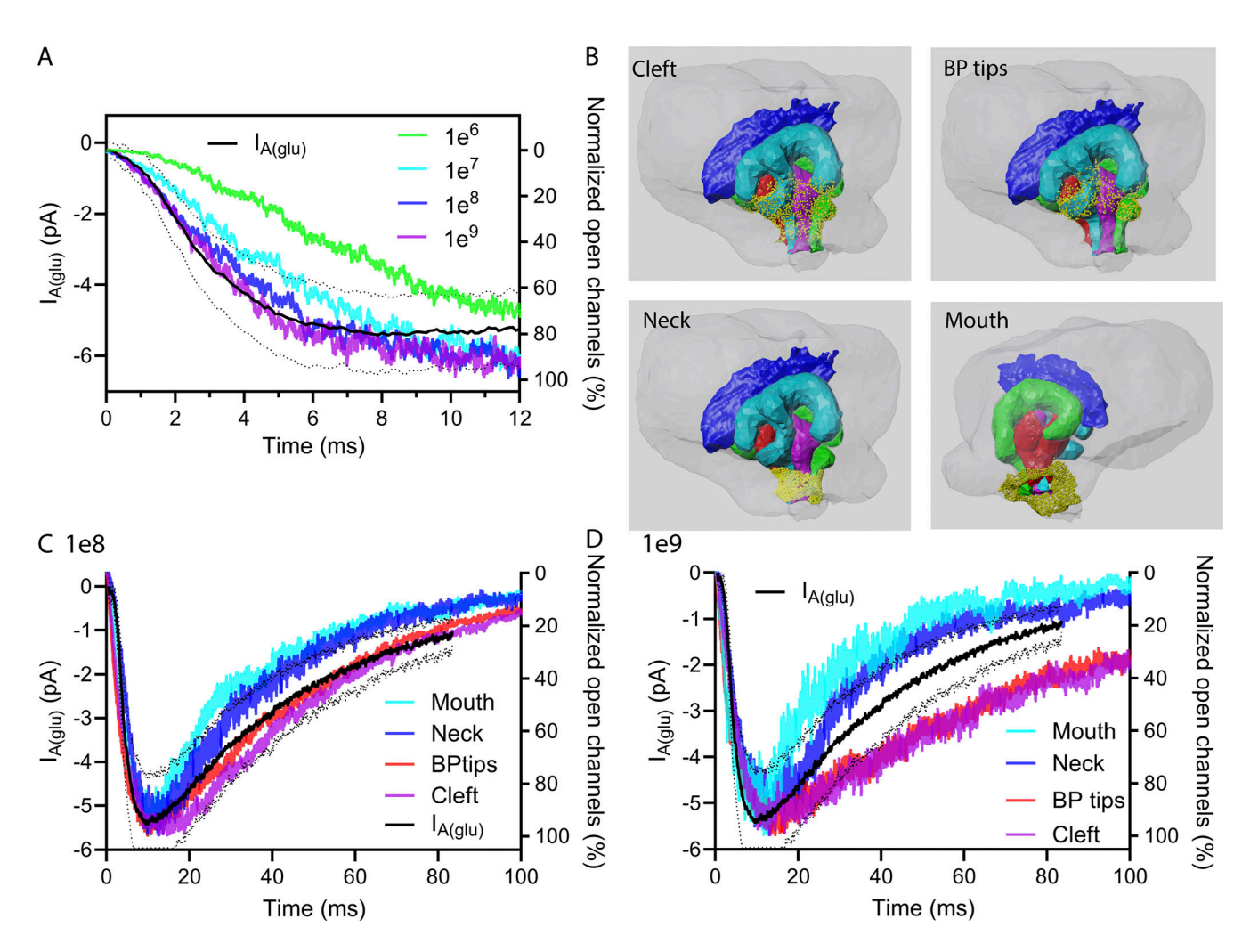


Figure S1. **EAAT5 parameters and placement. (A)** Comparison of ON rates for glutamate binding to EAAT5 (1×10^6 to 1×10^9 M/s). The black trace shows the average \pm SD single-vesicle $I_{A(glu)}$ in rods. **(B)** Illustration of EAAT5 (yellow puncta) placement in four different regions of the synaptic invagination: throughout the cleft (Cleft), adjacent to BP dendritic tips (BP tips), the neck of the invagination (Neck), and just outside the mouth of the invaginating synapse (Mouth). The ribbon is colored dark blue. HCs are shown in green and turquoise. RBPs are in red and purple. **(C)** Simulated EAAT5 anion channel activity after placing EAAT5 in the different regions shown in B with a glutamate ON-binding rate of 1×10^8 M/s. **(D)** Simulated EAAT5 anion channel activity with placement in various locations using an ON rate of 1×10^9 M/S. Traces show the average of 12 simulations run with different seed values.



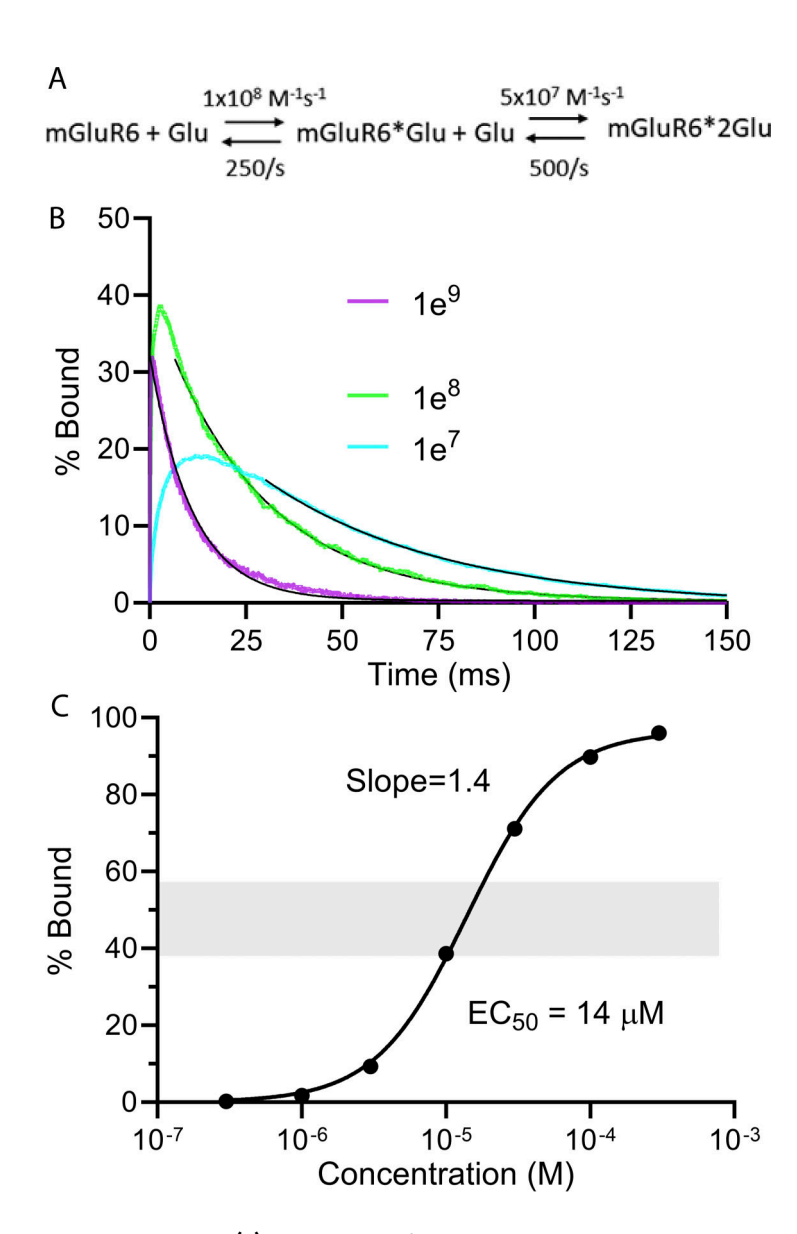


Figure S2. **Kinetics of glutamate binding to mGluR6. (A)** Kinetic scheme for glutamate binding to mGluR6. The activated receptor was considered the doubly bound state (mGluR6*2Glu). **(B)** Kinetics of mGluR6 activation (i.e., doubly bound mGluR6) is shown for different glutamate-binding rates. For 1×10^9 , 1×10^8 , and 1×10^7 M/s, the corresponding OFF rates for unbinding of the last glutamate molecule were 2,500/s, 250/s, and 25/s, respectively. The later portion of the decay was fit with a single exponential: 1×10^9 M/s, 1×10^8 M/s, 26.7 ms; 1×10^7 M/s, 46.7 ms. Simulations show the average of 12 seed values run in rod 3 in the presence of 3,000 EAAT5. **(C)** Plot of steady-state mGluR6 activation as a function of glutamate concentration using the model parameters in A. Data were fit with a sigmoidal Hill function: $EC_{50} = 14 \mu$ M. Hill slope = 1.4.